Structural degradation of thermal SiO_2 on Si by high-temperature annealing: Defect generation

A. Stesmans, B. Nouwen, and V. V. Afanas'ev
Department of Physics, University of Leuven, Celestijnenlaan 200D, 3001 Leuven, Belgium
(Received 27 July 2001; published 15 July 2002)

An electron spin resonance (ESR) study has been carried out of point defects generated in standard thermal SiO_2 on (100) Si during vacuum annealing in the temperature range $T_{an}=950-1250\,°C$, including the predominant exclusive *S* center in addition to the familiar E'_γ, E'_δ, and *EX* defects. The latter only appear after 10-eV optical excitation. The *S* and E'_γ density is found to increase monotonically with T_{an}, while *EX* and E'_δ detectivity fades for $T_{an}\geqslant 1050$ and 1200 °C, respectively. Over broad T_{an} ranges, the generation of all three defects *S*, E'_γ, and E'_δ appears thermally activated (Arrhenius type) with a common activation energy $E_a \approx 1.6$ eV. Large defect densities may be reached, i.e., [*S*] up to $\sim 1\times 10^{15}\,cm^{-2}$ for $T_{an}=1250\,°C$, typically one order of magnitude larger than $[E'_\gamma]$. With a view to identification, the *S*-center ESR characteristics have been mapped in detail. Its susceptibility is found nearly paramagnetic—Curie-Weiss type with critical temperature $T_c=1.3\pm 0.4$ K, indicative of a weak ferromagnetic coupling; the defects appear clustered. Oxide etch-back experiments reveal that during degradation the oxide undergoes significant modification, dependent on depth into the oxide film. As to defect distribution, for $T_{an}=1200\,°C$, the etch-back experiments show the *S* centers to predominantly occur near the oxide borders, with a sharp pileup within ~40 Å of the Si/SiO_2 interface, and a more stretched out one (~150 Å) towards the top surface; *S* and E'_γ centers generally occur in anticorrelation. The *S* defects are susceptible to passivation in molecular H_2. From the salient ESR properties, the *S* center is suggested to be of the type $Si_nO_{3-n}{\equiv}Si\cdot$ $(n=1,2)$. Though tentative, the observed weak hyperfine structure may be compatible with either the single $n=1$ defect or an overlap of both the $n=1,2$ types, the defect system exhibiting substantial randomness-induced variation in defect morphology. Based on the known interfacial SiO_2 reduction process, the thermal degradation of the oxide as a whole is interpreted as effectuated by interface-released SiO.

DOI: 10.1103/PhysRevB.66.045307 PACS number(s): 68.60.Dv, 76.30.Mi, 61.72.Ji, 85.30.De

I. INTRODUCTION

It is well established experimentally that some types of post-oxidation anneal (POA) treatments may lead to electrical degradation of thermal Si/SiO_2 structures.[1–4] Especially at high anneal temperatures T_{an} ($\gtrsim$600 °C) in an oxygen-deficient ambient, the effects of POA appear electrically detrimental.[5] It is accepted that the electrical degradation of the oxide layer is largely concerned with the introduction of defects. Yet the microscopic essence of part of the degradation process, in terms of point defect generation, was revealed only rather recently by detailed electron spin resonance (ESR) observations.[6–9]

In particular, at the (111) Si/SiO_2 (Ref. 7) and (100) Si/SiO_2 (Ref. 9) interfaces, degradation resulting from post-oxidation vacuum anneal (POVA) was identified as permanent additional creation of the P_b-type interface defects.[10] For the (111) Si/SiO_2 structure, it was found that the degradation process was initiated from $T_{an}\sim 640\,°C$ onward, exhibiting a monotone increase in P_b ($Si_3{\equiv}Si\cdot$) density above the inherent value[7] ($\sim 5\times 10^{12}$ cm^{-2}) present in the as-grown state as a result of mismatch.

These recent findings have unveiled the effects of POVA on the *interface* condition to atomic detail. In the present complementary study, we mainly intend to address the effects of POVA on the (bulk-)*oxide* layer. To this matter, as a possible starting point may serve a recent study on thermal SiO_2 exposed to POVA at $T_{an}\geqslant 950\,°C$,[6] reporting the generation of several types of ESR active point defects in the oxide. Perhaps most remarkable in this study is the observation of a new—at least, in thermal SiO_2—characteristic isotropic broad ESR signal at $g=2.0027$. On the basis of its salient ESR features, the signal was identified with the defect, labeled *S*, reported once in previous work on vacuum-annealed ($T\gtrsim 700$ K) fused silica glasses.[11] This terminology is further adopted here. Additionally, this *S* center generation during degradation was found attendant with the appearance of other, more familiar oxide point defects:[6] Together with *S*, the *EX* defect[12] was observed (*EX* has been suggested to be an electron delocalized over four oxygens at a Si vacancy site; cluster of nonbridging oxygen-related hole centers: NBOHC cluster). After applying vacuum ultraviolet (VUV) irradiation, E'_γ (generic entity[13] $O_3{\equiv}Si\cdot$) appeared, and VUV irradiation applied under a positive bias (+30 V) revealed also the presence of the related E'_δ defect.[14] Based on recent extensive calculations involving atomic-scale modeling, E'_δ is ascribed to an impaired electron delocalized over two neighboring, nearly equivalent Si atoms in the oxide (a symmetrical variant of the E'_γ center) at the site of a mono-oxygen vacancy,[15–17] although there is still experimental dispute.[18]

The abundant appearance of these oxide defects brings to the fore yet another structural aspect of the Si/SiO_2 degradation. The defects might be interpreted as ''reaction products'' of some kind of reaction in (rearrangement of) the oxide, and systematic observations of their occurrence might offer key information to the understanding of the microscopic kinetics

involved, an ultimate point of interest here.

A previous first hint at this kind of knowledge might be the suggestion the defect creation to be related to a more drastic oxide decomposition process, also observed under high-temperature vacuum conditions.[19] By the observation of the formation of pores (voids) through the SiO_2 film, the process was evidenced to occur via the freeing of volatile SiO at the Si/SiO_2 interface through the net reduction reaction $Si(s)+SiO_2(s)\rightarrow 2SiO$ (volatile). The *in situ* observation of $SiO(g)$ production under reduced O_2 pressure in a POA furnace[20] provided further evidence for this reaction. Additionally, outdiffusion and subsequent desorption of the volatile SiO from thermal Si/SiO_2 during POVA at 800 °C was evidenced through observation of significant changes in the profile of the so-called *suboxides* (i.e., $Si^{3+}\cdots Si^{0}$ states in SiO_2) monitored by angle-resolved x-ray photoelectron spectroscopy.[21] Also of importance for the present work is another study, where it was shown that *S* centers can be induced in pure quartz by annealing at ~1140 °C in the presence of $SiO(g)$ ambient—they remain absent, however, if annealed in vacuum.[22]

Additional insight into the oxide degradation scheme might follow from detailed knowledge of the structural origin and identity of the occurring defects. Obtaining such understanding is of considerable interest in the light of the key role the Si/SiO_2 structure occupies in current microelectronic devicing. Especially, the as-yet-unknown structure of the *S* center may provide useful information. Upon its first observation in P-doped silica glasses, the *S* center (termed *S* after *singlet*) was tentatively assigned to E'-like defects, with a modified backbond arrangement.[11] These defects—represented as $O_2Si{\equiv}Si\cdot$ and $OSi_2{\equiv}Si\cdot$—were suggested by Holzenkampfer *et al.*[23] to exist in SiO_x with $0\leqslant x\leqslant 2$. Though plausible, the presented interpretation based on the E' variants remains tentative and lacks conclusive experimental evidence. Basically, the structure of the *S* defect has so far remained elusive, essentially, because of the lack of data on ESR hyperfine structure and possible *g* anisotropy that prevents reliable assessment of its atomic nature.

The aim of the present study is to further explore the creation of defects associated with degradation of the oxide. Special attention is paid to their occurrence as a function of the POA temperature T_{an}, with main emphasis on the ESR characterization of the *S* defect.

II. EXPERIMENTAL DETAILS

Samples were obtained from commercial 2-in.-diam two-side polished float-zone (100) Si/SiO_2 wafers (~80 μm thick, 10–30 Ω cm, *p* type), fully processed in a technological facility.[24] Following standard RCA (Radio Corporation of America) cleaning, the wafers were oxidized to an oxide thickness $d_{ox}=66$ nm (1000 °C, 1 atm dry O_2), *in situ* succeeded by an N_2 anneal (N_2 flow, 30 min).

For ESR purposes, the wafers were cut in slices of 2×9 mm^2 main face. Subsequently, ESR samples, each comprising 7–10 slices, were submitted to POVA for ~1 h at different temperatures in the range 900–1250 °C. The POVA was terminated by cooling to room temperature in vacuum (quasiexponential, with cooling rate constant ~200 s). The treatments were carried out using a laboratory high-vacuum setup, leak tight to better then 10^{-10} Torr l/s. Details can be found elsewhere.[9]

After a first ESR test, the sample slices (both sides) were additionally exposed to VUV photons (10 eV, $\sim 10^{15}$ photons cm^{-2} s^{-1}, 300 s) utilizing a resonant Kr discharge lamp sealed with a MgF_2 window. One aim of this treatment is to maximally photodissociate H from passivated defects (ESR activation), thus optimally exposing the defect sites. The use of the relatively low photon energy, which exceeds the SiO_2 band gap by only ~1 eV, excludes the knockoff of Si or O atoms from oxide network sites. Semitransparent Au films (~10 nm thick), evaporated at both sides after the thermal treatments, were used to apply a positive bias during the 10-eV photon exposure. Standardly, +20 V was used, except for the $T_{an}=1250$ °C sample for which a +10 V bias was applied.

Conventional absorption-mode *K*-band (~20.5 GHz) ESR was performed in the range 4.2–35 K. The modulation amplitude (0.25 G, ~100 kHz) of the applied field **B** and microwave power P_μ incident on the TE_{011} cavity (of loaded quality factor $Q\sim 10\,000$) were adjusted to linear signal response levels. Spin densities were determined by comparison of the signal intensity *I* (obtained by double numerical integration of the measured absorption derivative spectra dP_μ/dB) to that of a comounted calibrated SiP *g* marker and spin standard ($g=1.998\,69$, spin $s=1/2$). Both signals were recorded in one trace. Taking into account geometrical factors and integration error, the absolute accuracy reached on the spin density is estimated at ~30%. Additional control measurements were carried out in a similar *Q*-band spectrometer set up operated at $T=5$–300 K. Further details on both spectrometer setups are given elsewhere.[25,26]

III. EXPERIMENTAL OBSERVATIONS

A. Degradation

1. Generation of defects; assessment

Examples of ESR signals appearing upon POVA at various T_{an}, followed by VUV under bias, are shown in Fig. 1. Probably most eye catching, in the left part of the figure, is the isotropic signal appearing at $g\cong 2.0027$ [indicated by (A) in Fig. 1], previously labeled *S*.[6,11] As evidenced by comparison to the marker signal (at $g=1.998\,69$), there is a drastic increase in *S* signal intensity with T_{an} increasing toward 1250 °C. With increasing *S* density, a marked increase in the peak-to-peak width ΔB_{pp} is noticed, in particular towards the $T_{an}=1250$ °C sample. The spectra shown were measured applying $P_\mu=2.5\,\mu$W at $T=4.2$ K, for which ESR conditions there was no sign of microwave saturation of the *S* signal. The line shape appears to remain approximately Lorentzian throughout the whole T_{an} range covered, yet a subtle asymmetry in the signals can be discerned. To illustrate, an optimized Lorentzian curve (+ symbols) is compared to the highest-density signal in Fig. 1. This may not appear so obvious for the lower T_{an} *S* signals, distorted by additional signals in the negative signal lobe [e.g., (B) in Fig.

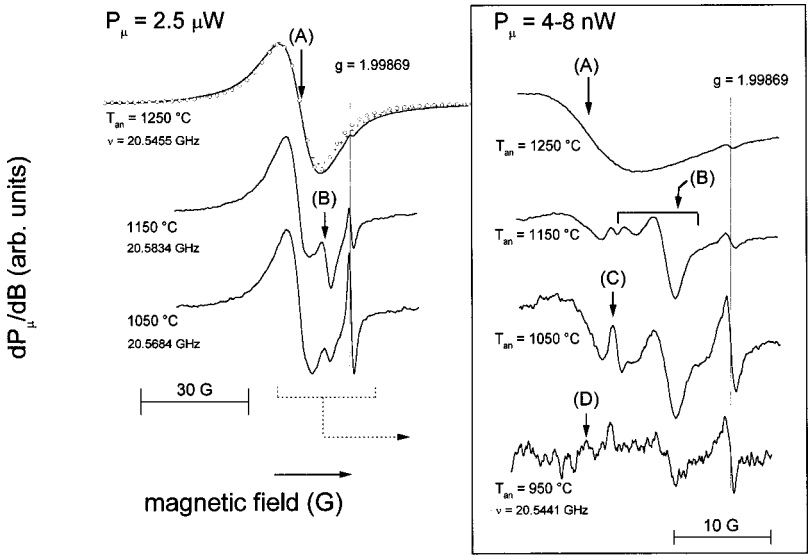

FIG. 1. *K*-band ESR spectra observed at 4.2 K in standard thermal Si/SiO_2 after ~1 h vacuum annealing at various temperatures T_{an}. The left part exposes the growth with increasing T_{an} of a broad signal (A) attributed to the *S* center. The right part (inset), magnifying the $g \sim 1.997-2.005$ region, was measured at lower microwave power to avoid saturation, thus correctly exposing the additional narrow signals, remaining partially saturated in the left side spectra. The signals (B) and (C) originate from E'_γ and E'_δ, respectively. Additionally, reproducible traces of the *EX* signal are observed (D). The + symbols represent a best Lorentzian fit to the largest intensity *S* signal. ○ symbols represent a tentative ''powder pattern'' fit assuming an axial dangling bond type defect (see text). The signal at $g = 1.998\,69$ stems from a comounted Si:P marker.

1]. However, it was observed that before VUV irradiation, when these additional signals are not detected, the *S* signal exhibits approximately the same characteristic weakly asymmetric signature.

Through optimization of the spectrometer settings and intense signal averaging, much effort was given to detect additional signals that could be attributed to hyperfine (hf) structure. Reproducible structures, albeit with limited resolution and obscured by interfering background signals, were observed at distances larger than ~40 G from the central Zeeman line. The assignment will be discussed below.

The ''distorting'' signals [e.g., (B)] appear to be saturated signals mainly due to E'_γ.[27] This is demonstrated in the inset of Fig. 1, closing in on the $g \approx 1.997-2.005$ window. Here saturation was avoided by reducing P_μ to 4–8 nW. Several signals can be recognized. The E'_γ signal displays a distinct powder pattern (PP) line shape and is most dominant [marked (B) in Fig. 1]. At $g = 2.0019$ an additional weak narrow line is observed [(C) in Fig. 1], also previously observed and attributed to the E'_δ defect. Finally, at $g = 2.0025$ another small narrow signal [(D)] appears reproducibly, which in line with previous observations is attributed to the *EX* center. It needs to be remarked, however, that the presence of *EX* in the presently studied series of samples is somewhat different from the previous observation.[6] In the latter study the distinct simultaneous presence of *EX* and *S* defects was observed (cf. Fig. 1 in Ref. 6), which, in the present study, was not observed.

Figure 2 shows the inferred areal densities of the observed defects *S*, E'_γ, E'_δ, and *EX* as a function of T_{an}. The quoted densities for all signals, including *S*, were obtained assuming spin $s = 1/2$ defects and Curie-type magnetic susceptibility. The densities were measured both before and after VUV irradiation. In the former case only the *S* signal could be discerned, appearing only for $T_{an} \geqslant 1050\,°C$. From this temperature on, the density of *S* (solid squares in Fig. 2) increases monotonically with increasing T_{an} up to 1200 °C. After the last T_{an} increment ($T_{an} = 1250\,°C$), an additional large increase (factor~10) in $[S]$ is observed, with some oxide degeneration also becoming visible optically. The distinct impact of the $T_{an} = 1250\,°C$ POVA step was also exposed electrically. Unlike all lower T_{an} samples ($\leqslant 1200\,°C$), it was noticed during VUV irradiation that the leakage current through the oxide upon applying the standard +20 V was very high (~1 mA/slice), which forced reduction of the biasing voltage to +10 V. Below $T_{an} = 1050\,°C$, weak traces of the signal near $g = 2.0027$ could only be observed in the $T_{an} = 1000\,°C$ sample. Possibly these traces are also due to *S*, but competition with the noise makes the integration troublesome. A rough estimate of the signal intensity would correspond to an areal density below $1 \times 10^{12}\,cm^{-2}$.

After VUV irradiation, the qualitative behavior of $[S]$ with T_{an} is approximately the same. However, an overall

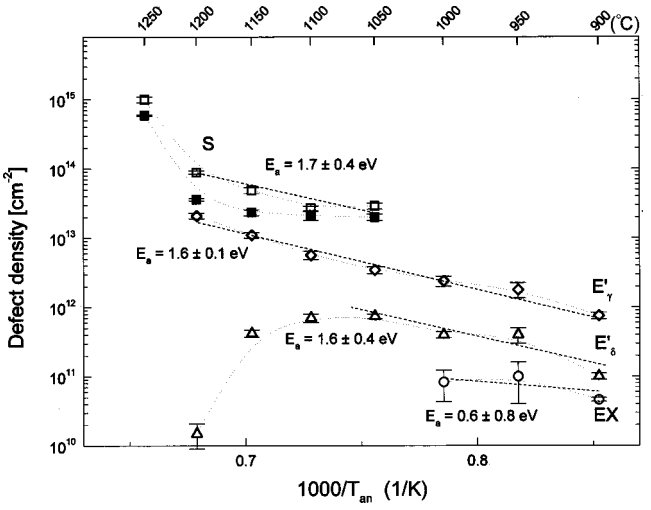

FIG. 2. Areal defect densities of *S* (□), E'_γ (◇), E'_δ (△), and *EX* (○) defects inferred from *K*-band ESR in standard thermal Si/SiO_2 after ~1 h vacuum anneal at various temperatures, before (solid symbols) and after VUV irradiation under positive bias (standardly +20 V). Dashed lines represent best fits of Eq. (9), from where the indicated activation energies (E_a) are inferred.

TABLE I. Evolution of the areal S and E'_γ defect densities over time. Quoted values are in units of $10^{13}\,\mathrm{cm}^{-2}$.

	T_{an}				
	1250 °C	1200 °C		1150 °C	
Condition	$[S]$	$[S]$	$[E'_\gamma]$	$[S]$	$[E'_\gamma]$
As-degraded	59 ± 1	3.60 ± 0.13		2.3 ± 0.25	
As-degraded+ VUV irr. biased	100 ± 10	8.9 ± 0.5	2.1 ± 0.2	4.9 ± 0.5	1.1 ± 0.1
As-degraded+ VUV irr. biased aged for ~3 years	47 ± 2.5	2.7 ± 0.25	0.68 ± 0.07	2.7 ± 0.1	0.34 ± 0.03

significant increase of the signal intensity, on average by a factor of ~1.8, is noticed.

The reported densities are in good agreement with the previous observation,[6] where $[S]\cong1.5\times10^{13}\,\mathrm{cm}^{-2}$ was reported for a sample as annealed at 1130 °C. In that study S was observed in samples annealed at T_{an} as low as 960 °C, for which $[S]$ was estimated $\leqslant1.5\times10^{12}\,\mathrm{cm}^{-2}$.

Upon VUV irradiation, also E'_γ, E'_δ, and EX do appear. E'_γ is most prominent among these. Its intensity increases steadily with increasing T_{an}, but remarkably, for the degenerate $T_{an}=1250$ °C sample, the E'_γ density drops below detectivity ($[E'_\gamma]<9\times10^{10}\,\mathrm{cm}^{-2}$). Approximately, a similar behavior is observed for the less populous E'_δ center. However, the E'_δ signal intensity diminishes rapidly for $T_{an}\gtrsim1100$ °C. As indicated, the EX signal is observed weakly and only when the S signal is absent. Considering that the observed intensities extend over several orders of magnitude, the loss of signal intensity of the various signals (E'_γ for $T_{an}>1200$ °C, E'_δ from $T_{an}\sim1100$ °C, EX for $T_{an}>1050$ °C) might partly be artificially induced by misinterpretation in the deconvolution of the various resonance signals.

2. Aging

Three of the highest-defect density samples were remeasured after being kept in standard laboratory conditions for ~3 years after the initial ESR tests. Table I compares the evolution of the obtained defect densities. Surprisingly, this reveals signs of aging, i.e., an overall decrease of the defect density by a factor of 2–3. Comparing the $T_{an}=1200$ and 1150 °C samples, it is interesting to note that the ratio $[S]/[E'_\gamma]$ remains comparable prior and after the decay for both samples. Attempts to reset the original defect density in the $T_{an}=1200$ °C sample, aged for ~3 years, by repeating the VUV irradiation failed: either with or without bias, the density remained essentially unaffected, except for an apparent small (~30%) increase in $[E'_\gamma]$ and the marginal reappearance of E'_δ.

3. Defect depth profile

A defect distribution depth profile was determined on an aged sample stack degraded at 1200 °C, exhibiting $[S]=2.7\pm0.25\times10^{13}\,\mathrm{cm}^{-2}$ ($4.1\times10^{18}\,\mathrm{cm}^{-3}$, uniform) after aging for about 3 years. This was carried out by sequentially thinning down the oxide for controlled times in diluted HF [HF(44%):H_2O, 1:9 (by volume)] stabilized at 21 °C, alternated with ESR signal intensity measurements. The thickness of the remaining oxide layer was determined by monochromatic ellipsometry, mostly on separate, but identically treated sample slices. Over the various etch-off steps, no significant changes in line shape, linewidth or position of the various signals were noticed. It may be useful to add that the 1200 °C POVA treatment had no impact on the initial oxide thickness: a value of $d_{ox}=663\pm6$ Å was measured both prior and after POVA.

Figure 3(a) shows the relation between the etch time and removed oxide thickness, together with the inferred values for the etch rate r_{HF}. For standard state-of-the-art thermal oxide, the etch rate would correspond to ~5.5 Å/s,[28] fairly uniform over the oxide. Clearly, the degraded oxide under study displays a nonuniform etch rate. Roughly, two regimes can be distinguished: In a first one, pertaining to the ~450-Å outer oxide layer, the etch rate can be approximated as being constant within the experimental error: The average value for r_{HF} is determined as 5.5 ± 0.7 Å/s, well in agreement with previous data.[28] Second, over the remaining ~210-Å oxide layer, a marked decrease in the etch rate towards the interface is noticed. For the ultimate ~50 Å, r_{HF} has decreased to ~0.4 Å/s, revealing a significant gradient in r_{HF}.

The depth profiles of the volume densities for S and E'_γ, denoted N_V^S and $N_V^{E'_\gamma}$, respectively, are shown in Figs. 3(b) and 3(c). These reveal that S centers are situated preferentially near the oxide surface and near the interface: Roughly half of the total amount of S centers resides within ~50 Å of either the outer oxide surface or the interface. The pileup of S at the interface, though, appears sharper than that at the oxide surface. In the bulk of the oxide, an apparent slight increase in N_V^S occurs in the region 300–400 Å from the interface. The observed depth profile complies with the previous observation where is was reported that $[S]$ was reduced by ~70% upon removing half the oxide layer.[6]

Remarkably, E'_γ appears to be present only in the top half of the oxide layer and reaches a maximum in $N_V^{E'_\gamma}$ at a depth

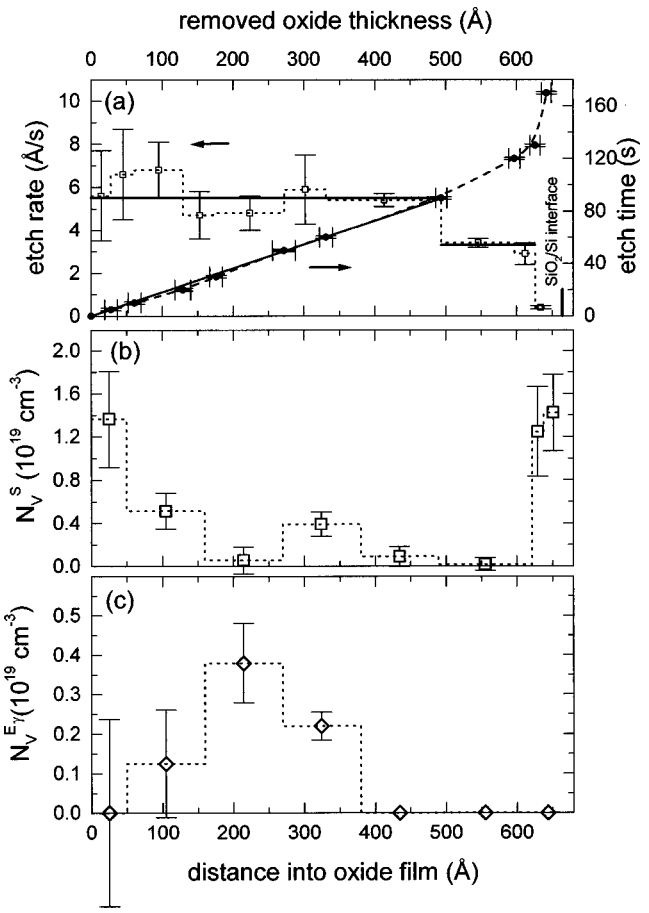

FIG. 3. (a) Etch time vs removed oxide thickness (●) for standard thermal Si/SiO_2 submitted to POVA at 1200 °C and inferred etch rate (□) as a function of depth into the oxide. Solid lines indicate ''constant'' approximation to the etch rate. Dashed line guides the eye. (b),(c) Distribution of the *S* and E'_γ volume defect densities N_V^S and $N_V^{E'_\gamma}$, respectively, over the oxide thickness. Dotted lines represent etch-back intervals over which was averaged.

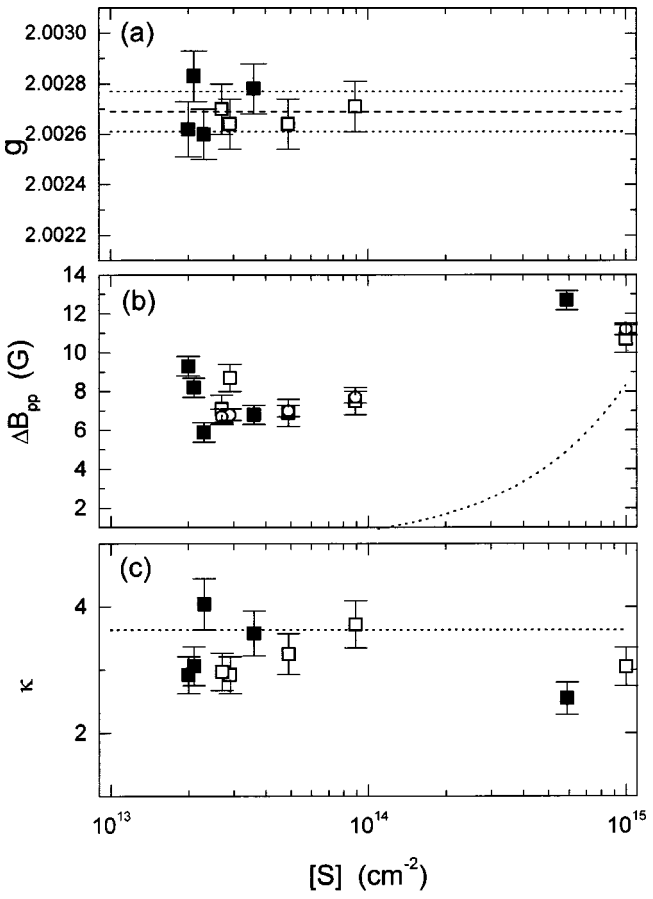

FIG. 4. Zero-crossing *g* value (a), peak-to-peak linewidth ΔB_{pp} (b), and line shape factor κ (c) of the *S*-center ESR signal as a function of the measured defect density: (□) *K*-band data (4.2 K), (○) *Q*-band (~33 GHz; 10 K). Solid and open symbols represent values obtained prior and after VUV irradiation under positive bias (+20 V), respectively. (a) The dashed and dotted lines indicate the average *g* value 2.002 69± 0.000 08 and error interval, respectively. (b) The curve here represents the calculated [see Refs. 39 and 40 and Eq. (4)] minimum expected dipolar broadening component assuming uniform defect distribution over the oxide thickness. (c) The dotted line marks the Lorentzian line shape factor $\kappa^L = 3.63$.

of ~210 Å. This behavior is unexpected as E'_γ is usually found distributed throughout the oxide with a distribution pronouncedly peaking towards the interface.[29] In comparing $N_V^{E'_\gamma}$ with N_V^S, it may be suggested that both defects roughly occur in anticorrelation.

B. *S*-center characterization

1. Salient ESR parameters

The behavior of the *g* value, ΔB_{pp}, and the line shape factor κ [defined as $\kappa \equiv I/(A \times \Delta B_{pp}^2)$, with *A* half the signal peak-to-peak height] of the *S* signal as a function of the areal density are summarized in Fig. 4.

Except for the highest *S*-density sample, the zero crossing *g* value behaves isotropic with respect to the direction of **B**. For this reason the *g* value for the former sample is not shown in Fig. 4(a). Within experimental error, *g* appears constant for all other samples. Apart from the fact that the data appear somewhat more scattered before VUV irradiation, no significant influence from the irradiation on *g* is noticed. Possibly, the influence of occurring unresolved resonance lines, due to, e.g., *EX*, might have contributed to such scatter. The averaged value obtained is $g = 2.002\,69 \pm 0.000\,08$.

The behavior of ΔB_{pp} for the *S* signal is depicted in Fig. 4(b). The *S* signal is unusually broad as compared to other generated defects (cf. *K* band: ΔB_{pp} intrinsic $E'_\gamma \sim 1$ G, $EX \sim 1$ G, $E'_\delta \sim 0.8$ G). A common trend clearly observable both before and after irradiation is a considerable broadening of ΔB_{pp} towards the highest density. Again, it may be noticed that there is a larger scatter in the data prior to VUV irradiation. The linewidth obtained from additional *Q*-band spectrometer (frequency $\nu \sim 33$ GHz, $T = 10$ K) control measurements on the irradiated samples are also indicated in Fig. 4(b) (open circles). Within experimental error the linewidth appears to be independent of ν.

The behavior of κ is shown in Fig. 4(c). Although no marked trend is observable here, it is clear that the dominating line shape broadening contribution is approximately

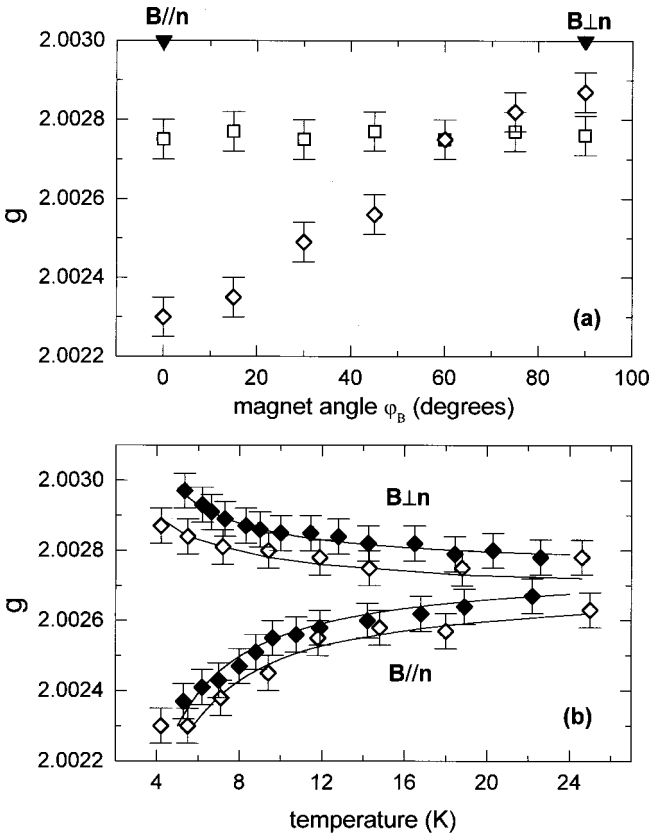

FIG. 5. (a) *K*-band angular behavior at 4.2 K of the *S* signal zero-crossing *g* value for two samples of different *S* density, determined as $\sim 47\times10^{13}\,\mathrm{cm}^{-2}$ (◇) and $2.7\times10^{13}\,\mathrm{cm}^{-2}$ (□). (b) Dependence of the extreme *g* values obtained for **B**∥**n** and **B**⊥**n** [see (a); ◇] on observational temperature at *K* (◇) and *Q* band (◆). Solid lines represent a best fit to the data based on the formulas for the Curie-Weiss susceptibility [Eqs. (1) and (2)] and the influence of demagnetizing fields [Eqs. (6) and (7)].

Lorentzian: Most of the determined line shape factors situate in the interval $\kappa=3-4$, i.e., close to the value $\kappa^L=3.63$. for a Lorentzian line.

A remarkable angular dependence of *g* on magnet angle φ_B (angle between **B** and the interface normal **n**) is observed for the highest-*S*-density sample. This is shown for $T=4.2$ K in Fig. 5, comparing the variation in *g* for a highest *S* density sample ($[S]=4.7\times10^{14}\,\mathrm{cm}^{-2}$, diamonds) with the isotropic behavior of a sample with $[S]=2.7\times10^{13}\,\mathrm{cm}^{-2}$ (squares). The relative accuracy in φ_B is estimated at $\sim0.2°$, yet there may be a larger shift in the absolute angle from **n**, possibly amounting to $\sim10°$. Figure 5(b) ($[S]=4\times10^{14}\,\mathrm{cm}^2$) shows the evolution of *g* at the extreme positions (i.e., **B**∥**n** and **B**⊥**n**) as a function of *T* at *K*(◇) and *Q* band (◆). Clearly, with increasing *T*, both extremes converge, albeit at a slightly different value for each ν and the anisotropy in *g* gradually fades.

The behavior of the *S* center line width ΔB_{pp} with *T* is shown in Fig. 6. There appears to be a slight trend to decrease with increasing *T*, most pronounced in the highest-density sample, displaying a decrease of ~1 G in ΔB_{pp} as *T* increases from ~4 to 25 K. For the other samples, this trend is less pronounced or just absent.

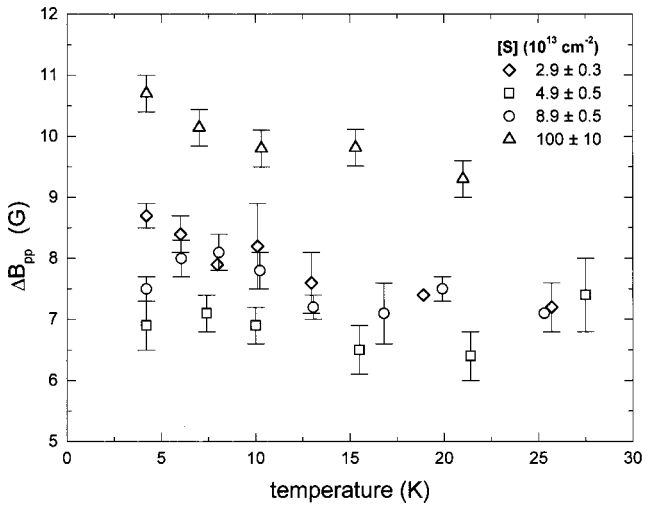

FIG. 6. Temperature dependence of ΔB_{pp} of the *S*-center *K*-band ESR signal for samples of different *S* concentration: 2.9 ± 0.3 (◇), 4.9 ± 0.5 (□), 8.9 ± 0.5 (○), and 100 ± 10 (△) $\times10^{13}\,\mathrm{cm}^{-2}$.

2. Magnetism of the S spin system

The magnetic susceptibility χ of the *S* spin system was determined for the four highest-*S*-density samples. This was done by measuring the signal intensity *I* as a function of *T* in the range 4.3–35 K. Generally, Curie-Weiss-type behavior is expected, i.e.,

$$I\sim\chi=\frac{C}{T-T_C}, \tag{1}$$

with T_C the Curie temperature and *C* the Curie constant, proportional to the volume spin density N_V, given by

$$C=\frac{\mu_0 N_V g^2\beta^2 s(s+1)}{3k_B}. \tag{2}$$

Here μ_0, k_B, β, and *s* are the magnetic permeability of the vacuum, Boltzmann constant, Bohr magneton, and spin of the magnetic particles, respectively.

The measured I^{-1} values are shown in Fig. 7. Solid lines represent best fits of Eq. (1) to the data. The thus inferred parameters *C* and T_C as a function of $[S]$ are shown in Fig. 8. As expected, *C* exhibits a quite linear proportionality with $[S]$. T_C appears constant within experimental error. An average value of 1.9 ± 0.7 K is obtained, indicating a slight trend to ferromagnetic coupling.

3. Interaction of the S center with hydrogen

It is a known fact that various types of point defects occurring in the Si/SiO_2 structure exhibit a prominent interaction with hydrogen in varying *T* ranges, e.g., passivation[30,31] into an electrically inactive (diamagnetic) state through bonding to H—a well-known fact for E'- and P_b-type defects. Accordingly, in an attempt to passivate *S* centers, a

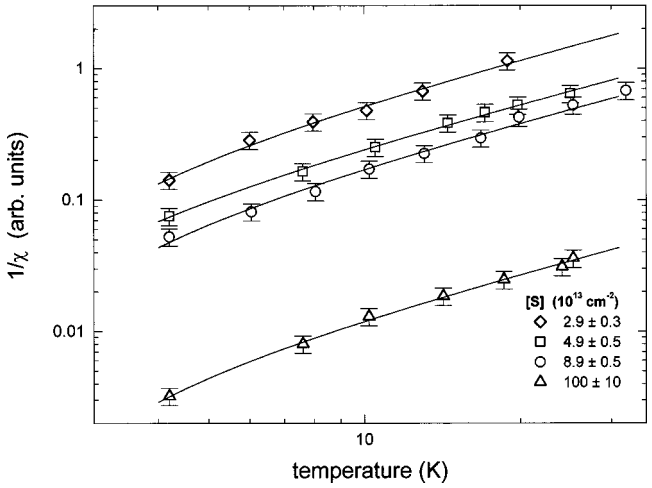

FIG. 7. Temperature dependence of the magnetic susceptibility of the *S* spin system for various densities: 2.9 ± 0.3 (◇), 4.9 ± 0.5 (□), 8.9 ± 0.3 (○), and 100 ± 10 (△) $\times10^{13}\,\mathrm{cm}^{-2}$. The defects were induced by POVA of standard Si/SiO_2 at various temperatures. The solid lines represent best fits of expression (1).

limited study was carried out by subjecting two samples exhibiting *S* signals to additional thermal treatments in molecular hydrogen (1 atm). A first sample (○ in Fig. 9), having received a POVA at 1150 °C for 69 min, was submitted to successive isochronal thermal treatments (~100 min) in H_2 at increasing temperatures (T_{H_2}) of 500, 670, and 770 °C. Additionally, a final anneal at 670 °C in H_2 for 124 min was applied. The normalized ESR areal density of *S* defects is shown in Fig. 9. Clearly, the anneals affect the observed [*S*], exposing passivation. After a steady, strong initial decrease, the density of the ESR-active *S* centers levels off, perhaps even appearing to increase again for $T_{H_2}>650\,°C$. Apparently, also, a final anneal step again at $T_{H_2}=670\,°C$, though on the edge of experimental error, does not quite result in

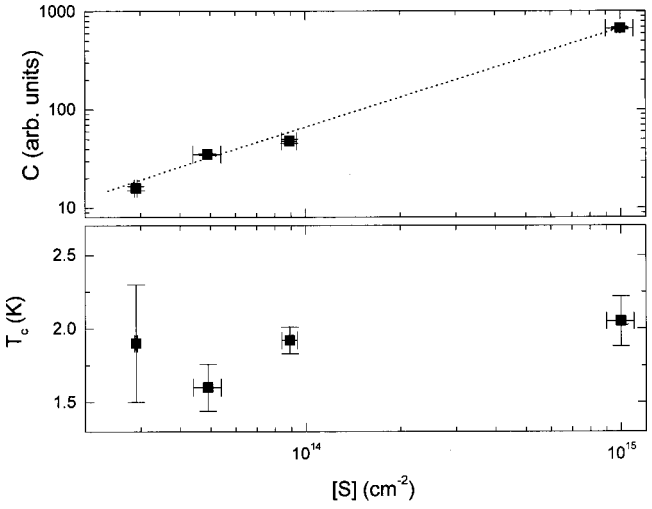

FIG. 8. Curie constant *C* and Curie temperature T_C as a function of areal *S* density, as inferred from fitting the temperature dependence of the magnetic susceptibility for the various densities (cf. Fig. 7).

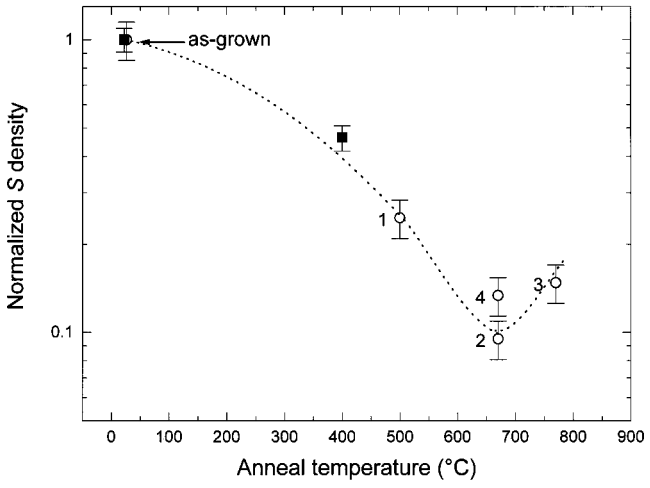

FIG. 9. Evolution of the normalized *S* defect density upon isochronal (~100 min) annealing in H_2 at various temperatures (○). The initial *S* density was set by POVA of the Si/SiO_2 structure at 1150 °C for 69 min. Numbers refer to the successive anneal treatments carried out at 500 °C (1), 670 °C (2), 770 °C (3), and 670 °C (124 min) (4). Solid symbols show the effect on the observed *S* density of a 400 °C anneal (38 min) in H_2 on a Si/SiO_2 structure submitted to POVA at 1100 °C for 69 min with Al (thickness: 500 Å) evaporated on top of the oxide.

reproducing the previous $T_{H_2}=670\,°C$ anneal density. A second sample (■ in Fig. 9), vacuum annealed at $T_{an}=1100\,°C$ for 69 min, received an anneal in H_2 (400 °C, 38 min) after an Al layer (thickness 500 ± 25 Å) was evaporated onto the oxide. It is known that during subsequent heating *atomic* hydrogen is released at the Al/SiO_2 interface—the latter is presumed to be produced by Al reacting at the interface with trace amounts of water, more specifically, bound hydroxyl groups, absorbed before the Al layer deposition[32,33] (suggested reaction Al+OH→AlO+H). However, as shown in Fig. 9, there appears no effect of the metallization.

Probably, the safe interpretation here is that, within experimental accuracy, the *S* defects may be passivated to a residual value, i.e., ~10% of the *S* centers left unpassivated, inaccessible for passivation in H_2 for some physical reason, at least in the T_{an}-time window covered. One reason could be the existence of a substantial spread in the activation energy for passivation,[31] as discussed below.

IV. ANALYSIS AND DISCUSSION

A. *S* center

1. Previous observations

Previously, the *S* center was already reported as a defect residing in the oxide layer,[6] fully confirmed here. The main experimental evidence then was the observed reduction (~70%) of the signal intensity after etch-off of approximately half of the 66-nm-thick oxide layer. The more detailed etch-off data presented in this work confirm this observation both qualitatively and quantitatively. Moreover, the *S* signal was also observed in high-purity quartz.[22]

Because of the high (technological) sample quality used for the previous[6,22] and present observations and the fact that *S* has been observed in samples of various origin,[6,11,22] we may exclude the possibility that any impurity other than the omnipresent H is involved in the *S* defect structure on the basis of the deduced defect densities: For one, in the case of the highest-density sample, the areal density ($\sim 1 \times 10^{15}\,\mathrm{cm}^{-2}$) corresponds to a volume density $N_V^S = 1.5 \times 10^{20}\,\mathrm{cm}^{-3}$ if assuming a uniform defect distribution and no oxide ablation. With $\sim 2.3 \times 10^{22}$ SiO_2 groups per cm^3, an impurity as a central part of the *S* structure would require an impurity content in the oxide amounting to the few at. per mile level.

It has been suggested previously that the *S* center pertains to structural defects of the type $O_2Si{\equiv}Si\cdot$ and/or $OSi_2{\equiv}Si\cdot$,[11] i.e., an intermediate defect structure between the known $Si_3{\equiv}Si\cdot$ (P_b) and $O_3{\equiv}Si\cdot$ (E'_γ) trivalent Si centers. These defects were first suggested by Holzenkampfer *et al.*[23] to explain the behavior of ESR spectra observed in amorphous SiO_x with $0 \leqslant x \leqslant 2$, prepared by electron-beam evaporation under different oxygen pressures. As x decreased, the intensity of the ESR signal component due to the E'_γ center decreased. A new (compound) component gradually emerged with a g value greater than that of the E'_γ center. Its intensity and g value increased further with decreasing x. For $x < 0.2$ the g value was equal to that observed for the signals in the spectra of amorphous Si attributed to the $Si_3{\equiv}Si\cdot$ defect (*D* center). The continuously changing g and line shape were attributed to changes in the relative population of the mentioned $Si_nO_{3-n}{\equiv}Si\cdot$ ($n = 1-3$) type centers.

Interestingly, systematic theoretical quantum-mechanical analysis of hf coupling constants, electronic structure, and electrical properties for such neutral $Si_nO_{3-n}{\equiv}Si\cdot$ radicals with $n = 0, \ldots, 3$ have since become available.[34,35] These calculations, based on *ab initio* Hartree-Fock theory, obtain fairly accurately ($\sim$10%–20%) the measured hf splitting for the dominant ^{29}Si (apex defected atom) hf doublet for the P_b and E'_γ defects, i.e., the $n = 3$ and $n = 0$ clusters, respectively. Accordingly, partly because of these predictions, *in the present study*, an extensive search for *S*-center hf structure has been carried out—with limited success, however (*vide infra*).

Very relevant for the present work may be that a defect, observed in both Cr- and Si-implanted SiO_2 glasses, was also attributed to $O_2Si{\equiv}Si\cdot$ and/or $OSi_2{\equiv}Si\cdot$ type of defects.[36,37] It is interesting to note how salient ESR features of that defect, termed *X* and described as a ''E'-type defect associated with a Si-Si homobond,'' resemble those of the presently investigated *S* center. Like *S*, the center is described as exhibiting an ''almost isotropic [ESR] line shape,'' i.e., displaying a similar characteristic slightly asymmetric signature (cf. Fig. 2 of Ref. 36) with a ΔB_{pp} of 8 G (Ref. 36) to 9 G (Ref. 37). The signal is reported not to saturate appreciably up to power levels of 200 mW at 110 K for *X*-band ESR. So the *X* and *S* signals might be suggested to pertain to one and the same defect. Yet there is a marked difference in g, reported at 2.0022 ± 0.0001 for *X* vis á vis 2.00269 ± 0.00008 for the *S* center. Perhaps, though, this difference in g is only seemingly. Possibly, it could, at least partly, be explained by referring to the observed variations in g as a function of the magnet field angle and local defect density (see Sec. III B 1), which apparently were not varied in the *X* signal studies. However, this possibility has to be dropped as, unlike the Cr^+ implantation work where v-SiO_2 plates were used, crushed samples were used for ESR in the Si^+-ion implantation work, both studies reporting the same g ($=2.0022$) value (*vide infra*). Instead, it may be noticed that the difference in the reported g values corresponds to differences in the resonance zero crossing field of only $\sim$0.8 G (*X* band) and $\sim$1.6 G (*K* band). Considering that both studies suffered from the presence of interfering signals, like, E'_γ and the peroxy radical (PR),[37] and given the large linewidths of the *S* and *X* signals, the difference in the determined resonance position (and *a fortiori* g) might then rather concern an artifact. Yet, as will be outlined later, we do not deem the *X* and *S* centers to be identical, so the difference in reported g values is considered significant.

Pertinently, in the $^{29}Si^+$-ion implantation work on v-SiO_2,[37] a doublet of 230 G was detected, which on grounds of hf considerations of AB_3 radicals and Si-implantation-tied effects, was ascribed to hf structure of apex ^{29}Si nuclei of $Si_nO_{3-n}{\equiv}Si\cdot$ ($n = 1,2$) centers. Also the (central) *X* signal was observed (though not explicitly referred to that way). For clarity, though, it needs to be remarked that no explicit correlation of the 230-G doublet and the (central) *X* signal was advanced, neither interpretatively nor experimentally: no correlation in g or intensity (variation) was demonstrated—an absolute requirement for the signals to be treated as one spectrum, originating from one defect. Likely, in a correct scientific attitude, this was not attempted due to experimental complexity and limits. In subsequent theoretical work,[34] the 230-G splitting was found close to the calculated dominant ^{29}Si splitting, i.e., A_{iso} $[= T_r(\hat{A})/3]$ ~ 250 G, where $\hat{A}$ is the *hf* tensor, for the $O_2Si{\equiv}Si\cdot$ defect, from where *X* was identified with this center. (Continuing the stated terminology, then, the $OSi_2{\equiv}Si\cdot$ defect was designated as a *Y* center. As far as is known, this defect has not been experimentally isolated yet.) Implicitly, here, the 230-G doublet and *X* were assumed to be correlated. So, in strict terms, while the assignment of the $O_2Si{\equiv}Si\cdot$ defect as originating the 230-G doublet may be correct, it may just not be related with the (central) *X* signal at all. In the initial report[6] on the *S* signal in thermal SiO_2, observation of a doublet of $\sim$270 G splitting was mentioned; yet, as explicitly stated, exploration of the correlation was experimentally prevented. In the theoretical work,[34] from the close hf splitting values, *S* was also ranked as an $O_2Si{\equiv}Si\cdot$ defect and, *a fortiori*, as an *X* center. Clearly, identification demands the utmost care: Solid experimental ground must be provided as to the (isotopic) intensity correlation and variation of Zeeman and hf signals. If absent, firm identification is excluded.

2. Linewidth and shape

If, as likely, the *S* center concerns an intrinsic oxide defect, a remarkable observation is that, compared to the other observed oxide defects, the *S* signal linewidth is unusually large and the signal intensity may reach high values. More-

over, the *S* signal appears to be considerably less saturable (cf. Fig. 1) than other known oxide point defects.

Yet these characteristics may be put in a plausible perspective by taking into account the dipole-dipole (DD) interactions between the defect spins. Indeed, DD interactions would contribute to explaining the unusually large width and the linewidth variations with $[S]$ due to the characteristic broadening effects.[38] Also, the DD interaction represents an energetic coupling between the spins that enhances the drain of absorbed microwave energy, hence explaining the lower ESR saturability of the *S* spin system as compared to other typical oxide defects. Furthermore, the observed independence of the linewidth on observational frequency (cf. Fig. 4) and the Lorentzian shape of the ESR signal also comply with the effects expected from DD interactions.

The successful theory developed by Van Vleck[38] and Kittel and Abrahams[39] allows one to quantitatively estimate the density-dependent broadening contribution due to DD interactions. Among others, it predicts that for spin $s=1/2$ centers, randomly distributed over a cubic lattice of lattice constant d, with $\mathbf{B}\perp[001]$ axis and a fractional occupancy $f<0.01$, the line shape for the dipolar contribution is a (cutoff) Lorentzian with a peak-to-peak width given by

$$\Delta B_{pp}\ \ (\mathrm{G}) = \frac{2}{\sqrt{3}} \times 5.41 f \frac{g\beta}{d^3} = 1.16 \times 10^{-19} N_V\ \ (\mathrm{cm}^{-3}). \tag{3}$$

In the case of randomly distributed centers, like *S*, this expression is modified[40] to

$$\Delta B_{pp}\ \ (\mathrm{G}) = 0.54 \times 10^{-19} N_V^S\ \ (\mathrm{cm}^{-3}). \tag{4}$$

The modification accounts for the random defect positioning and orientation leading to a reduction of ΔB_{pp} by a factor of 0.71. Additionally, a factor of 2/3 has been incorporated accounting for the supposed anisotropy in g (see also below).

The expected DD contribution is minimal when the average distance between the defects is maximized, i.e., if it is assumed that *S* centers are uniformly distributed over the oxide thickness. In that case, Eq. (4) can also be expressed as a function of the corresponding areal density (using $N_V^S = [S]/d_{\mathrm{ox}}$). The thus obtained curve is shown in Fig. 4(b) (dotted curve), from where it appears that over the whole density range, the calculated values are significantly smaller than the observed ΔB_{pp}. The discrepancy may have two causes. First, if still accepting the DD interaction as dominant broadening mechanism, it must imply the local N_V^S value to be significantly higher than inferred based on the assumption of a uniform distribution throughout the oxide. This appears evidenced by the nonuniform defect distribution in Fig. 3, suggesting agglomeration of *S* centers and thus locally enhanced effective N_V^S values. Second, additional line broadening mechanisms are still expected to be present.

In Fig. 4(b) it is seen that for $[S]$ increasing from $\sim 1 \times 10^{14}$ cm^{-2} (equivalent to $1.5 \times 10^{19}\,\mathrm{cm}^{-3}$ if uniformly distributed) an increase in ΔB_{pp} of $\sim$4 G is measured toward $[S] = 1 \times 10^{15}$ cm^{-2} (uniform volume density $\sim 1.5 \times 10^{20}$ cm^{-3}). This increasing trend is also followed by the expected minimum dipolar contribution for uniform distribution (dotted curve). As to this broadening, it appears as if the experimental and theoretical data converge for the highest *S* densities. This then may suggest that, toward the higher densities, the defect distribution becomes more uniform. However, in the range below $[S] \sim 1 \times 10^{14}$ cm^{-2}, the minimum expected dipolar contribution is rather negligible (<1 G), compared to the experimentally observed ΔB_{pp}. It is seen that ΔB_{pp} changes little (almost constant) in this region, which would then indicate, if assuming that ΔB_{pp} is determined by DD interactions, *local agglomeration* (clustering) of the *S* defects effectively resulting in an approximately constant local volume density over a range of $[S]$ values (see also below).

Generally, several line broadening mechanisms can be expected to contribute. Considering that the *S* center originates from an oxide defect, it may be interesting to estimate the extent to which g anisotropy in the amorphous SiO_2, i.e., the so-called PP effect, contributes to the linewidth. Here it needs to be remarked that, in order to calculate the minimum dipolar contribution [cf. Eq. (4)], g anisotropy was already assumed to be present, as this is the most general case. Importantly, if no g anisotropy is present, the minimum dipolar contribution [cf. Fig. 4(b)] would increase by a factor of 3/2.[40] At the highest *S* density, such an increase in the minimum dipolar contribution, i.e., from 8.1 to 12.2 G, would exceed the experimentally observed value $\Delta B_{pp} = 11$ G. In a simplifying view, this suggests that g anisotropy would be required to match the data. Yet it should be added that this kind of straightforward reasoning may be illegitimate, as the line shape structure may represent the combined effect of several broadening mechanisms, which, in general, do not add linearly.

The absence of an explicit PP line shape suggests that any occurring anisotropy in g provides only a minor contribution to the total linewidth. However, PP effects could possibly be the cause of the typically observed subtle asymmetry of the line shape. Accordingly, an attempt to fit the observed signal for the highest-density sample with a PP structure was carried out. Two basic assumptions were made. First, the g dyadic was restricted to axial symmetry. Within the limits of acceptable fitting, the difference between the two components $g_\parallel$ and $g_\perp$ was maximized to obtain the *worst case scenario* anisotropy in g value. Second, the residual contribution ΔB_{pp}^R, representing the combined effect of all other line broadening mechanisms, was also allowed to display axial anisotropy. Particularly, the residual contribution $\Delta B_{pp}^{R,\parallel}$ along the axial $g_\parallel$ direction, was restricted to $\Delta B_{pp}^{R,\perp} \geqslant \Delta B_{pp}^{R,\parallel}$, where $\Delta B_{pp}^{R,\perp}$ represents the residual broadening contribution along any direction perpendicular to $g_\parallel$, i.e., along $g_\perp$. Both assumptions comply with the expected behavior of a dangling bond (DB) type of defect, as outlined by Watkins and Corbet[41] and, among others, was successfully applied to the case of P_b.[42] The additional contribution to ΔB_{pp}^R in the perpendicular direction is attributed to strain-induced variations in g, known to primarily result in a spread in $g_\perp$, but not to first order in $g_\parallel$. Usually, the broadening contribution due to such perturbations on the g dyadic, henceforth called *strain broadening*, is assumed to be Gaussian. However, the simulations bore out that the residual line

for the *S* center should rather be taken Lorentzian. This result, again, is expected when DD interactions dominate the residual broadening. The optimized fit, shown in Fig. 1 (○ symbol), represents a better fit than the single Lorentzian line (+ symbols in Fig. 1) in the central part. In the wings, however, the fit still fails, probably due to the specific dipolar line shape effects.[39] The inferred g components are $g_{\parallel}=2.001\,70\pm0.000\,10$ and $g_{\perp}=2.003\,35\pm0.000\,10$, while for the residual contributions, $\Delta B_{pp}^{R,\parallel}=6.8\pm0.5$ G and $\Delta B_{pp}^{R,\perp}=10.8\pm0.5$ G are obtained. These values should be handled with reservation as they are the result of a tentative fitting of a nonprominent PP shape, and the uniqueness of the result is in doubt. However, albeit arguably, the values may add insight into the structure of the resonance line. Among others, the simulation demonstrates that even without clearly resolved PP shape features being observed, the difference between $g_{\parallel}$ and $g_{\perp}$ can amount to $\sim1\times10^{-3}$ (cf. E'_{γ}: $g_{\perp}-g_{\parallel}=1.2\times10^{-3}$; P_b: $g_{\perp}-g_{\parallel}=7.3\times10^{-3}$).

In line with the inferred g anisotropy, the difference between the residual linewidth contribution for the $g_{\parallel}$ and $g_{\perp}$ directions could be interpreted as due to strain broadening. Here in a first approximation we might neglect the strain broadening contribution in $\Delta B_{pp}^{R,\parallel}$ (Refs. 41 and 42) and take the linear difference $\Delta B_{pp}^{R,\perp}-\Delta B_{pp}^{R,\parallel}=4.0\pm0.7$ G as a measure for the additional strain broadening contribution on $g_{\perp}$ as compared to $g_{\parallel}$. Assuming the latter to be Gaussian, an estimate of $\sigma_{g_{\perp}}$, the standard deviation in $g_{\perp}$, can be obtained from[42]

$$\Delta B_{pp}^{R,\perp}-\Delta B_{pp}^{R,\parallel}\approx\frac{2h\nu}{\beta g_{\perp}^{2}}\sigma_{\perp}\,. \tag{5}$$

This results in $\sigma_{g_{\perp}}\approx0.000\,55\pm0.000\,10$, an intermediate result as compared to the values for, e.g., P_b ($\sigma_{g_{\perp}}=0.000\,74$) (Refs. 42–44) and E'_{γ} ($\sigma_{g_{\perp}}\sim0.000\,16$) (Ref. 45).

3. Angular dependence of resonance field

Another peculiar observation for the *S* center is the angular dependence of the zero-crossing field value, observed for the highest-*S* density sample only (cf. Fig. 5). Generally, this is not expected for an amorphous material where microscopic defect anisotropy like, e.g., g anisotropy (resonance position), is averaged out orientationally. Hinted by the fact that it is only observed for the highest [*S*] sample in the present case, the origin of the angular dependence in g is attributed to demagnetization, i.e., situated at a more macroscopic level. The effects of demagnetizing fields are well known in ferromagnetic and superconducting materials.[46] In ESR, demagnetization effects can often be neglected, yet small shifts in g of paramagnetic spin systems may become significant.[47,48]

The impact of demagnetization effects depends on the applied magnetic field direction, sample shape,[49] and magnetization. For the simple case of a disk-shaped sample, it is found that for $\chi(T)\ll1$ (SI units)

$$g(T)\simeq g_{\mathrm{ref}}\left[1+\frac{1}{2}\chi(T)\right]\quad\text{for }\mathbf{B}\perp\mathbf{n}, \tag{6}$$

$$g(T)\simeq g_{\mathrm{ref}}[1-\chi(T)]\quad\text{for }\mathbf{B}\parallel\mathbf{n}. \tag{7}$$

Here g_{ref} represents the "high-temperature" g value. Combining Eqs. (6) and (7) with Eqs. (1) and (2) allowed successful fitting of the temperature dependence of g for both orientations of **B**, as shown in Fig. 5(b) (curves). The inferred parameters from the fitting are $g_{\mathrm{ref}}=2.002\,69\pm0.000\,02$, $T_C=0.8\pm0.5$ K, $N_V^S=(10.6\pm0.8)\times10^{19}\,\mathrm{cm}^{-3}$, and $g_{\mathrm{ref}}=2.00275\pm0.00002$, $T_c=1.3\pm0.5$ K, $N_V^s=(10.2\pm08)\pm10^{19}\,\mathrm{cm}^{-3}$ for *K* and *Q* band, respectively. The slight shift in measured g (zero crossing) between *K* and *Q* band (cf. constant vertical shift in Fig. 5(b) corresponding to ~0.2 G at *K* band), not expected from Eqs. (6) and (7), may concern a line-shape effect (powder pattern).

When comparing results, excellent agreement is thus found with the g value measured for the lower-density samples [g (*K*-band) $=2.002\,69\pm0.000\,08$ and g (*Q* band) $=2.00275\pm0.00008$]. Both values of T_c, i.e., 0.8 and 1.3 K, appear somewhat lower than the value $T_C=1.9\pm0.7$ K obtained from the signal intensity measurements. Yet both measurements in unison indicate a very low T_C, with average value of 1.3 ± 0.4 K. The obtained value of $N_V^S=10.6\times10^{19}\,\mathrm{cm}^{-3}$ cannot be compared to a directly obtained estimate of the *local* N_V^S (not measured). Yet as an extreme upper limit it may be compared to an N_V^S estimate based on Eq. (4) and the observed total linewidth $\Delta B_{pp}=11$ G, giving a maximum $N_V^S\approx20\times10^{19}\,\mathrm{cm}^{-3}$. The obtained value from fitting Eqs. (6) and (7) stays well below this upper limit. As a lower limit, on the other hand, the value $N_V^S=10.6\times10^{19}\,\mathrm{cm}^{-3}$ may be compared to $N_V^S=(7.2\pm0.4)\times10^{19}\,\mathrm{cm}^{-3}$, i.e., the volume density inferred from the areal density ($\sim47\times10^{13}\,\mathrm{cm}^{-2}$) assuming a uniform defect distribution over d_{ox}.

For the $T_{\mathrm{an}}=1200\,^{\circ}\mathrm{C}$ case ($[S]\sim2.7\times10^{13}\,\mathrm{cm}^{-2}$) of which the g-vs-φ_B behavior is shown as well [Fig. 5(a)], there is also a good agreement between the different approaches to N_V^S inference. For this sample, assuming that the defects occur in layers, the fitting using Eqs. (6) and (7) bears out that $N_V^S\lesssim(1.3\pm0.1)\times10^{19}\,\mathrm{cm}^{-3}$. Larger values of N_V^S would lead to observable anisotropy in $g(\gtrsim3\times10^{-5})$. Additionally, for this sample, a direct estimate for the local densities is available (see Fig. 3). A maximum local value of $N_V^S=1.4\pm0.4\times10^{19}\,\mathrm{cm}^{-3}$ was obtained—within experimental error in good agreement with the results of the demagnetization. Both values are about a factor of ~10 below the upper limit based on ΔB_{pp} (~7 G) and Eq. (4) which would require $N_V^S\lesssim(13\pm1)\times10^{19}\,\mathrm{cm}^{-3}$.

In comparing the different approaches to the density determination, some remarks may be added concerning the origin of the linewidth and the defect distribution. First, it may be noticed that for the $T_{\mathrm{an}}=1200$ and $=1250\,^{\circ}\mathrm{C}$ samples, it is found that the *uniform* N_V^S values, obtained for [*S*] assuming uniform distribution over d_{ox}, i.e., $(0.40\pm0.04)\times10^{19}$ and $(7.2\pm0.4)\times10^{19}\,\mathrm{cm}^{-3}$, respectively, are significantly smaller than their local N_V^S values, determined as $\sim1.4\times10^{19}\,\mathrm{cm}^{-3}$ (via depth profiling) and $\sim10.6\times10^{19}\,\mathrm{cm}^{-3}$ (via demagnetization), respectively. This indicates that *S* centers probably occur aggregated in both samples. Yet it appears that this aggregation is more pronounced in the $T_{\mathrm{an}}=1200\,^{\circ}\mathrm{C}$ sample where the ratio between "maximum" and

uniform values is ~3.5 vis-á-vis ~1.5 for the $T_{an}=1250\,^{\circ}C$ sample. This is in line with the comparison of the ΔB_{pp}-vs-$[S]$ profile with the minimally expected dipolar contribution [cf. Fig. 4(b)], where it was already suggested that towards the highest S density the defect distribution becomes more uniform.

There are two more remarks. First, it may be noted that for the $T_{an}=1200\,^{\circ}C$ sample, the maximum N_V^S value obtained from analysis of the demagnetization effects [$(1.3\pm0.1)\times10^{19}\,cm^{-3}$] is almost equal to the maximum N_V^S obtained from the depth profiling, $\sim1.4\times10^{19}\,cm^{-3}$. At first sight, this would leave little room for clustering of defects within regions considerably smaller than the etch steps. Yet the possibility that clusters may have shapes that are less sensitive to demagnetization effects (e.g., spherical) makes conclusions less straightforward in this case. It may be added that such a scenario in which S centers are predominantly clustered to result in more or less constant local volume densities with varying $[S]$ also complies with the fact that no significant dependence of T_C on $[S]$ was found. Second, it is remarked that the inferred volume densities for both samples are significantly smaller than the upper limits obtained on the basis of the dipolar broadening formula [Eq. (4)] and the linewidth. This suggests that other line broadening mechanisms may also be of importance.

4. Depth profile

As shown in Fig. 3(a), the oxide etch rate is not uniform as a function of the depth into the oxide, with r_{HF} decreasing inward from 5.5 ± 0.7 to ~0.4 Å/s—more than an order of magnitude. As known, this may be related to changes in the stoichiometry and/or the structure of the oxide.[50] The drastic decrease, then, apparently reveals that in the ~200-Å-thick interfacial oxide layer significant deviations from the standard oxide occur, the deviation growing towards the interface. In support, it was also noticed that in approaching this region the surface of the remaining oxide layer changed from wetting in H_2O (typical for standard SiO_2) to nonwetting (typical for a virgin Si surface).

An interesting observation is that the etch rate appears partly mirrored in the S-center distribution: It is noticed that close to the interface where r_{HF} reaches a minimum, a pileup of S centers is observed. Additionally, a weaker fluctuation in N_V^S is noticed at a depth in the oxide of ~320 Å, i.e., approaching at the transition region between the *regular* and the likely gradually *altering* oxide.

Clearly, though, the correlation between r_{HF} and N_V^S is not tight, as the pileup of S centers towards the outer surface—albeit more gradual than near the Si/SiO_2 interface—is not attended by a significant change in r_{HF}.

5. hf structure

a. Basic results. Key to atomic defect characterization is the observation of ESR signals originating from hf interactions. In this respect, ESR has proved indispensible to providing insight into the chemical and structural nature of point defects. If admitting that S pertains to an intrinsic structural oxide defect, the possible atoms expected as immediate building blocks of the S defect are Si, O, and the ubiquitous H. Considering the natural abundances of isotopes with nuclear spin $I\neq0$, it may be assumed that only Si (^{29}Si, $I=1/2$, 4.7% natural abundance) and H (^{1}H, $I=1/2$, 99.985%) would have a reasonably detectable fraction of spin-active nuclei, unlike O (^{17}O, $I=5/2$, 0.037%). So through optimization of spectrometer settings and intense signal averaging, much effort was given to resolving additional hf doublets, with limited success, however: With the attained (maximum) number of S centers in a typical ESR sample ($\sim10^{15}$), no prominent hf structure could be discerned, the search further suffering from (known) interfering cavity background signals.

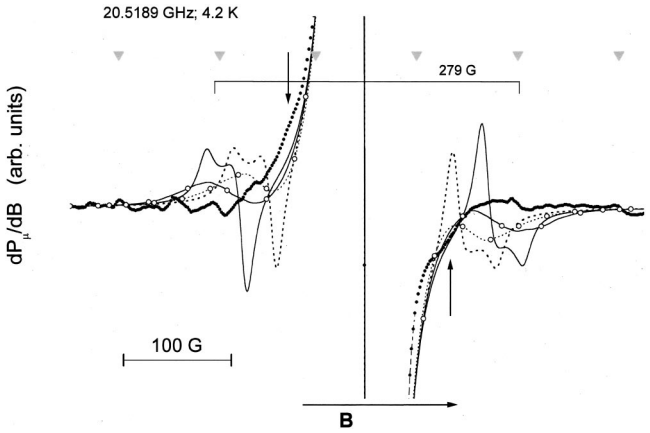

FIG. 10. Comparison of the wing structure of a K-band ESR S signal [(●)$[S]\sim10^{15}\,cm^{-2}$] observed at 4.3 K ($P_\mu\sim50$ nW) to theoretical hf structures predicted for the $O_2Si{\equiv}Si\cdot$ (thin solid lines) and $OSi_2{\equiv}Si\cdot$ (dotted lines) models, using hf splitting values from Ref. 34, rounded to axial symmetry. An isotropic g value of 2.002 69 was assumed. Additionally shown is the effect on the theoretical spectra of a 30% Gaussian spread on the components of $\hat{A}$ (solid and dotted lines marked with ○). The left wing of the measured spectrum was corrected for a broad background signal. ▼ symbols indicate a cavity background sextet, likely originating from Mn^{2+} impurities.

For reasons of ESR sensitivity and low-T accessibility, this search was most intensively carried using K-band ESR. So the discussion is started from there. Though weak, some structure is observed in the magnified wings of the intense central Zeeman signal of the K-band spectrum (bold dotted curve) shown in Fig. 10. The spectrum was observed at ~4.3 K on a Si/SiO_2 sample submitted to POVA at $T_{an}=1250\,^{\circ}C$ of $[S]\sim1\times10^{15}\,cm^{-2}$, the highest density obtained in this work. A doublet may be discerned, characterized, within the sizable uncertainty of the experiment, by a splitting of 279 ± 12 G and centered at the main (central) S Zeeman line; the signals (best exposed by the high-field one) are distinctly broadened, i.e., $\Delta B_{pp}\sim30$ G, as compared to the central signal ($\Delta B_{pp}\sim10.5$ G). As indicated, signals from a cavity background sextet (marked by solid triangles), ascribed to Mn^{2+} impurities, do interfere. In addition, a large, broad (~150 G) cavity background signal at the low-field side was substracted, potentially marring the low-field doublet signal even further.

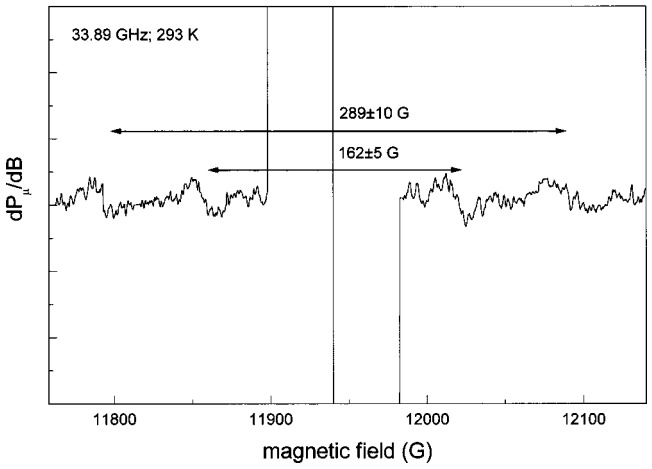

FIG. 11. Strongly magnified *Q*-band spectrum, observed at 293 K ($P_\mu = 2.97$ mW) after intense signal averaging and corrected for cavity background signals. After base line substraction two doublets appear, centered at the central *S* signal, with splittings of 162 ± 5 and 289 ± 10 G. The doublet signals are broadened compared to the *S* signal width.

On closer examination, as indicated by the arrows in Fig. 10, there may be even evidence for the presence of a second weak inner hf doublet, apparently also centered (within experimental accuracy) at the Zeeman-line zero crossing. It is generally observed for the highest-*S*-density samples (yet with variable resolution). However, even more than the previously hinted at doublet, the interpretation is hindered by the steep flanks of the central line and the (relative) signal weakness. So its mentioning situates perhaps even more on a tentative level. This obscures conclusive isolation, e.g., as regards its relationship to the *S* center, exact doublet splitting, signal width, and, perhaps of most interest of all, their signal intensity relative to that of the central line (isotopic abundance). In fact, attempting to do so may be at the edge of scientific rigor. Nevertheless, to mark an impression, a computer-aided substraction of a Lorentzian central signal has been carried out, from where a doublet splitting (zero crossing) of 162 ± 5 G and a hf linewidth 15 ± 3 G—i.e., smaller than of the outer doublet (30 G)—is estimated. Thus, even more so than for the first doublet, the involvement of this apparent second doublet with the *S* center is to be looked at with extreme caution. Nevertheless, for brevity, we shall henceforth refer to the doublets as the outer and inner hf structure, respectively.

To resolve the potential hf structure, the *S* signal has also been intensively averaged using *Q*-band spectrometry. An ultimate strongly magnified *Q*-band spectrum, observed at 293 K after intense signal averaging and corrected for cavity background signals, is displayed in Fig. 11, where it is rewarding to retrieve the signatures of both doublets, generally within the limits of experimental accuracy, of similar properties as exposed by the *K*-band data. In fact, the spectral values quoted for both doublets are rather averages of the *K*- and *Q*-band results. In the same breath, though, it needs to be added that as a result of the necessary applied invasive corrections for marring background signals, salient hf signal properties such as width, shape, and relative intensity may not have been correctly preserved. So the interpretation should be looked at with extreme caution. From combination of the *K*- and *Q*-band results, the ratio in spectral intensity Π (area under absorption curves) of the inner and outer doublets is estimated at ~ 0.6, with an experimental uncertainty>factor 2; the similar ratio $R = \Pi_{hf}/\Pi_z$ of the outer doublet to the central Zeeman signal may be ~ 0.015 (uncertainty factor 2). So within the large experimental uncertainty, the intensities of both doublets may be comparable.

Clearly, more discriminative experimental information will be needed to fully assess these doublets, which may partly come from further enhancement of the S/N ratio.

b. Nature of the S center. In one opinion, one may take the failure to detect prominent hf structure as evidence for the *S* center being an O-centric defect. However, the spectral features of the *S* signal are very dissimilar from those of known O-related defect centers, like the NBOHC (the $\equiv$Si-O$\cdot$ fragment[51]), peroxyradical ($\equiv$Si-O-O$\cdot$ fragment[52]), or even self-trapped holes.[53] Among others, all these centers display resolved powder pattern spectra with at least one component of the *g* dyadic significantly larger than (close to 2.010) the free-electron value $g_0 = 2.0023$. Moreover, these defects are easily annealed out and are not expected to occur in oxides annealed above $T_{an} = 950\,^\circ$C. So we rather adhere to the model that *S* concerns Si dangling bond type centers.

In another view then, (Si) hf signals may occur, but appear disproportionally weak because of excessive line broadening due to, e.g., hf anisotropy and/or strain effects. Effects of site-to-site variations in defect morphology are well expected in an amorphous medium (*vide supra*, discussion of linewidth). This possibility has been scrutinized at somewhat more detail within the context of the $Si_nO_{3-n}\equiv$Si$\cdot$ ($n = 1,2$) picture. Some of it is exemplified in Fig. 10 showing the simulated PP spectra for the $Si_nO_{3-n}\equiv$Si$\cdot$ ($n = 1,2$) type defects including ^{29}Si hf (interaction with one Si site, 4.7% ^{29}Si abundance) as predicted by Karna and Kurta[34] (thin solid curves represent the $n = 1$ case, dotted curves the case $n = 2$). The theoretically reported values were slightly rounded to obtain an axially symmetric hf tensor resulting in $A_\parallel = 294$ G and $A_\perp = 224$ G for the $n = 1$ defect and $A_\parallel = 245$ G and $A_\perp = 169$ G for $n = 2$. The central line was approximated by a single Lorentzian line and optimized to the observed central Zeeman signal. Clearly, the ^{29}Si hf structure in the wings of the theoretical spectra is relatively more peaky than any of the structures observed in the background. To explore further, Fig. 10 displays simulated hf spectra resulting from an assumed 30% Gaussian spread on the above-mentioned components of the $\hat{A}$ tensors [solid ($n = 1$) and dotted ($n = 2$) curves marked with ○], mimicing site-to-site variations in the defect bath. These hf structures expose an obvious broadening and, particularly in the neater high-field wing, the hf signal amplitudes are now comparable to the observed additional structure.

One may wish to compare this fairly large spread of 30% on $\hat{A}$-tensor components with that of other relevant defects in a-SiO_2. For the E' center in fused SiO_2, generically perhaps most closely related to the *S* center, a (Gaussian) spread $\Delta A_{iso} \sim 7\%$ on the isotropic part of the hf interaction

has been reported,[54] while for the P_b defect ($Si_3{\equiv}Si\cdot$), spreads $\Delta A_{iso}{\sim}10\%$ and 14% are found for standard thermal[55] (111) Si/SiO_2 ($T_{ox}=900\,°C$) and (111) Si/native oxide structures,[56] respectively. Thus, while acceptable, the spread for the present *S* case may appear somewhat larger. If admitting that the *S* signal arises from a $Si_nO_{3-n}{\equiv}Si\cdot$ ($n=1,2$) type center, one reason for enhanced spread in A_{iso} might be enhanced chemical atomic asymmetry, i.e., either 1Si/2O or 2Si/1O as tetrahadral base plane atoms as compared to E'_γ (3 O atoms) or P_b (3 Si atoms). Since $A_{iso} \propto |\Psi_s(0)|^2$ (wave function overlap of the unpaired spin at constituent atoms), the ''asymmetric'' situation is likely more prone to excessive broadening of the hf signals induced by vitreous disorder. Thus enhanced *S* hf line broadening may appear natural. In summary, while inconclusive, there may be evidence for ^{29}Si hf structure in the *S* signal's wings in expected regions.

With the information attained, albeit limited and plagued by experimental uncertainty, one may explore the significance as to the *S* center's atomic nature. Using the $Si_nO_{3-n}{\equiv}Si\cdot$ model(s) as backdrop, we assume $s=1/2$ for the *S* center. If deemed sufficiently reliable, two doublets are observed. Clearly, their splittings and relative positions exclude them from constituting one quadruplet originating from hf interaction of the unpaired electron with a single site of nuclear spin $I=3/2$. Likewise, their appearance as part of a sextet is excluded. So, likely, each doublet stems from an interaction of the unpaired spin with a single $I=1/2$ nuclear site. Then, within experimental uncertainty, the doublets may be part of (perhaps only one) or not part of the Si-defect spectrum. Obviously, with respect to the *S* center's origin, we can only further the discussion if accepting the former case. Next, if we assume that for each doublet the exposed relative spectral, within experimental accuracy, complies with the electron hf interaction with a single Si site of 4.7% natural ^{29}Si occupation (expected $R=0.049$), then, within the $Si_nO_{3-n}{\equiv}Si\cdot$ ($n=1,2$) picture, the finding could imply two things. In one interpretation, it could indicate the *S* signal to be a (balanced) superposition of the signals of both $O_2Si{\equiv}Si\cdot$ and $OSi_2{\equiv}Si\cdot$ defects. In that case, the intensity of both doublets may differ, as might be slightly suggested by the data. Also, in that case, with overlapping Zeeman signals one expects *R* to be (significantly) smaller (depending on $[O_2Si{\equiv}Si\cdot]/[OSi_2{\equiv}Si\cdot]$) than 0.049, the value for interaction with one ^{29}Si site—as suggested by the data also. Instead, if inferring from the data the doublets to be of equal intensity, it would rather favor the one-defect origin, i.e., $O_2Si{\equiv}Si\cdot$, where the two Si sites involved might originate two doublets. The data may favor somewhat the first interpretation. But, apparently, this is as far as the present interpretation can go. Obviously, in addition to further theoretical exploration, the decisive verdict has to come from improved experimental assessment, implying signal enhancement and controlled defect density variation. Until then, one cannot consider the *S* center (neither the *X* center) as identified.

6. Interaction with hydrogen

If, as suggested, *S* concerns a Si dangling bond type defect, distinct interactions with H_2 at appropriate elevated temperatures are to be expected. Depending on the S-H bond strength a passivation and depassivation scheme such as inferred for, e.g., P_b, could be envisaged.[30,31] However, as borne out by experiments, only part of the total *S* ensemble can be passivated: a fraction ~10% remains ESR active at ~670 °C. With T_{an} increasing to ~760 °C, even a slight recovery of the ESR-active fraction is discerned. But as stated, that finding may be at the limit of experimental reproducibility.

A possible explanation here could invoke the existence of substantial spreads σ_{E_f} and σ_{E_d} in the activation energies E_f and E_d for passivation and dissociation, respectively. For defects in an amorphous surrounding, σ_{E_f} and σ_{E_d} could turn out to be significantly larger as compared to, e.g., the values obtained for the P_b's ($\sigma_E/E=3\%-4\%$), rather pertaining to the crystalline Si substrate. With large spreads, there may be a non-negligible overlap of the (Gaussian) distributions in E_f and E_d. So the total *S* bath would indeed never become fully passivated. The behavior, then, would closely resemble the simultaneous action of passivation and dissociation as reported for the P_b defect[57] and the essence of the kinetics is outlined in more detail there. In fact, for the same reason, the P_b bath can never be 100% passivated in H_2. If correct, this finding will be of much significance as to the possibility of curing thermally induced degradation damage through the omnipracticed method of passivation of defects by hydrogen. But, clearly, the effect needs more in-depth investigation.

B. Degradation

1. Basic mechanism

Finally, we turn to the degradation process as a whole. As hinted at the Introduction, the previous observations[19,20,21] of the formation of gaseous SiO probably generated at the Si/SiO_2 interface and escaping into the disintegrating oxide layer towards the ambient during POVA might provide insight. The direct relevance of the presence of SiO for the appearance of defects, at least *S* centers, was demonstrated by POA studies on pure quartz: POA treatments in the presence of SiO caused the *S* signal to appear, while annealing quartz in vacuum did not induce any ESR signal.[22] The importance of the experiment is twofold: It isolates SiO as a critical ingredient required to generate *S* and reveals that the Si/SiO_2 interface plays a crucial role. The net interfacial decomposition reaction suggested to occur is

$$Si^{substrate}(s)+SiO_2^{oxide}(s)\rightarrow 2SiO(g)^{\uparrow}, \tag{8}$$

where the partial O_2 pressure p_{O_2} during POA drives the equilibrium condition: Beyond a critical value,[20] i.e., $p_{O_2} > 100 p_{SiO}^{equi}$, where p_{SiO}^{equi} represents the partial equilibrium SiO vapor pressure for reaction (8), the equilibrium is driven to the left, effectively resulting in oxide formation (possible via the reaction $2SiO+O_2\rightarrow 2SiO_2$). Importantly, complete disintegration of the oxide can be attained at elevated *T*. In surface science, this is a generally practiced method to obtain a virgin Si surface.[19] The occurrence of this reaction has been compellingly evidenced in conjunction by various ana-

lyzing methods[5,19,21] and the interfacial generation of SiO(g) has been invoked as a basic agent in accounting for various thermally induced effects on the Si/SiO_2 structure including catalytic effects on the thermomigration of impurities in SiO_2,[58] SiO-driven vacancy supersaturation in Si during annealing in Ar,[59] low-electric-field oxide breakdown,[5] thermal decomposition of (thin) oxide layers,[60] and γ-irradiation-induced E'_δ defect generation in buried oxide ($Si/SiO_2/Si$ sandwich) structures.[61]

In the light of these previous results, it appears natural to propose that the observed generation of defects is either related to the chemical reaction steps responsible for freeing SiO from the Si/SiO_2 interface *per se* or is the result of the interaction processes occurring while (reactive) SiO diffuses into the oxide. This quest was left unaddressed in Ref. 61. The latter interpretation is favored by the observation of *S*-center generation in quartz,[22] i.e., in the absence of an interface. Whatever the case, it may be important to remark that the samples studied here may be considered as being in a quenched momentary condition, providing an instantaneous view of the disintegrated oxide at the various T_{an} covered. Thus the observed, apparently unique, relation between the various densities of defects observed and T_{an} represents a (quenched-in) temperature-dependent dynamical steady state. Since the applied annealing time ($\sim$1 h) is long, this may also represent equilibrium conditions for each particular T_{an} value.

Assuming then that the generation of *S* is predominantly governed by the reaction between diffusing SiO and the SiO_2 network rather than to the initial freeing of SiO at the interface, we may address the observed depth profile for *S* defects. Regions of enhanced N_V^S are found near the interface and outer oxide surface. There is also a less-pronounced peak found in a region about 100 Å thick at $\sim$300 Å away from the interface.

From this picture, one may conclude that SiO molecules are produced at the Si/SiO_2 interface through reduction of SiO_2 by Si, which, in diffusing to the outer surface, are gradually consumed through reaction with appropriate sites in the oxide network, resulting in defect generation, e.g., *S*-center creation. In such a scenario the expected *S*-center distribution would exhibit an exponential type decay of N_V^S away from the Si/SiO_2 interface,[21] i.e., N_V^S peaking towards the Si/SiO_2 interface, as observed. The expected N_V^S-vs-depth distribution in the oxide layer would then be much like the one found for the E'_γ defect in as-grown standard Si/SiO_2.[29]

However, in this scenario, the trend of gradual increasing N_V^S towards the outer surface—albeit significantly more stretched out than near the Si/SiO_2 interface—is not understood. It may also appear in conflict with a result in Ref. 21. However, to be noted here is that in the latter work, POVA treatments were only performed up to 800 °C. But this does not necessarily mean that the basics of the simple model are wrong, as various additional effects may play a role. First, there is the fact that the initial undamaged oxide may not be homogeneous in depth, as the observed variations in the etch rate r_{HF} would suggest.[50] This may affect the oxide-network SiO interaction efficiency as well as the SiO diffusivity. So the effectuated N_V^S distribution during POVA may also partly be reminiscent of initial physicochemical variations in the oxide. If the SiO diffusivity would be affected, the less-pronounced peaking of N_V^S near the middle of the oxide might then involve a region of reduced SiO diffusivity. In this respect, one may refer to the presumed presence of pores[62] (dynamic channels) in dry thermal oxide and underlying pseudo-''crystallinity'' of the oxide.[63] Second, oxide modification (near-surface SiO sink) may also promote a gradual pileup of N_V^S towards the outer SiO_2 surface. Third, the interpretation has so far left out the possible drastic effect of H, omnipresent in thermal oxide [$\sim$10 ppm (Ref. 64) in dry SiO_2], known to have a hand in virtually every relevant aspect of the Si/SiO_2 structure.

Focusing on the quantitative aspects of the defect distribution, it was concluded that, if admitting that the linewidth is mainly determined dipolarly, the defects appear clustered. This then would comply with the previous observation where the POVA decomposition of thermal SiO_2 was reported to be highly nonuniform.[19] Also, the possibility of enhanced diffusion pathways, resulting in effective channeling of the SiO flow, may be envisaged.[62]

The measured depth profile of the E'_γ center is depicted in Fig. 3(c). As shown, no detectable amount of E'_γ could be traced near the SiO_2 borders. This is most remarkable in comparison with the case of standard thermal oxide (nondegraded) where an exponential-like distribution, peaking towards the interface, is observed.[29] If relating *S*-center creation to the interaction of volatile reactive SiO with the SiO_2 network, the stoichiometry at the *S*-defect site may be expected to be Si enriched. This then would put the anticorrelation between *S* and E'_γ in perspective. If both centers have oxygen deficiency in common, a competition in their presence might appear natural. Yet in the near interfacial region at 50–300 Å from the interface, neither *S* nor E'_γ appears present. Apparently, the structure or stoichiometry of this region disfavors the presence of defects after degradation.

Quantitative aspects suggest a common origin of the generation of the various defects. When the defect densities, as observed after VUV excitation, are plotted (logarithmically) versus reciprocal absolute anneal temperature as depicted in Fig. 2, linear dependences are revealed for the various defects, at least over part of the covered T_{an} range. Thus, in principle, it is possible to assign a thermal activation energy E_a to each defect, which may be obtained from the plots in Fig. 2 via the Arrhenius-type equation for a defect density n

$$n \propto \exp \frac{-E_a}{k_B T}. \tag{9}$$

Importantly, this formula has only a real physical meaning for equilibrium situations. It thus appears that for each set of data the observed defect density versus T_{an} behavior obeys Eq. (9), at least within a certain T_{an} interval. The best fits over the various intervals, together with the obtained corresponding values for E_a, are marked in Fig. 2. For *EX* the value of E_a is rather tentative and may be somewhat underestimated due to a lack of data points and large experimental uncertainties. Apart from the latter, it is interesting to note

that the obtained E_a values of other defects (S, E'_γ, E'_δ) are approximately equal, averaging to a value of $E_a \sim 1.6$ eV. This result suggests an intimate relationship between the mechanism(s) originating the various defects. Suggestively, the T dependence of the rate limiting step is the same over the various defects, hinting that it could be the same step for all three (four) defects.

We also remark that in other previous work,[65] where poly-Si-capped oxide layers were annealed in vacuum, resulting in the observation of E'_γ after UV irradiation under bias, a value $E_a = 1.5 \pm 0.1$ eV was reported for the occurring E'_γ defects. Finally, however suggestive and convenient, we would like to stress that the E_a values inferred here are only used to empirically quantify the observed density-vs-T_{an} dependence. Great care should be exercised in applying Eq. (9). Its physical background is not considered proved to be appropriate to describe the observed phenomena as may be testified by the applicability of the formula over only limited T ranges (cf. Fig. 2).

2. Reactive sites

Clearly, the nature of the rate limiting step for defect generation is a basic issue. One hint may come from the observed E_a values. Indeed, to be noticed is that, should the S center, as suggested, indeed be of the type $Si_nO_{3-n} \equiv Si\cdot$ ($n = 1,2$), all three defects S, E'_γ, and E'_δ of similar E_a are O-vacancy-related defects. As previously mentioned, EX is a distinctly different kind of defect, which may account for its weak appearance and strongly deviating E_a. Within the interfacial SiO release concept, this observation may be put in the perspective of the notion that incorporation of SiO in the SiO_2 network effectively constitutes Si enrichment. This may hint at the rate limiting step implying the effective incorporation of SiO at available reactive sites in the SiO_2 network, effectuating local network modifications of which at least one resembles that of O-vacancy formation, i.e., strained Si-Si or Si dangling bond formation. Clearly, about the very atomistic scenario of such a crucial step, ESR is of scant help as it only provides information about the end result, i.e., the presence of paramagnetic (dangling bond defects). So one can only speculate and one may envisage various possibilities.

A corrollary with the advanced picture is that, if the SiO-oxide network interaction would proceed sufficiently drastically (as may indeed be attained as, e.g., evidenced by effectuated total electrical degradation of the oxide[5]), it will affect virtually every fundamental aspect of the SiO_2 film, such as density, dielectric constant, local vibrational modes, chemical properties, etc., all of which have been reported. The presently observed drastic variation in the etch rate in dilute HF may constitute further pertinent evidence.

One more consequence of this (drastic) SiO-oxide interaction model is that distinct variations may be anticipated in the impact of heat treatment in O-deficient ambient over differently grown and handled thermal oxides. It is likely that SiO incorporation predominantly, if not exclusively, occurs at particular precursor sites present in the oxide prior to POVA. So if a difference in interaction sites is initially present, the outcome of POVA will vary accordingly. And there are numerous reports of physicochemical variations in thermal oxide films depending on growth conditions and postoxidation treatment, e.g., different (pore) structure between wet and dry oxidation, underlying pseudocrystalline structure of the oxide, chemical resistance, molar volume, Si-O-Si bridging bond angle distribution, etc. Further stretching the interpretation, it may thus even appear POVA may just serve as a kind of evaluation test of (thermal) oxide: dissimilarities in accessible SiO interaction precursor sites will be exposed.

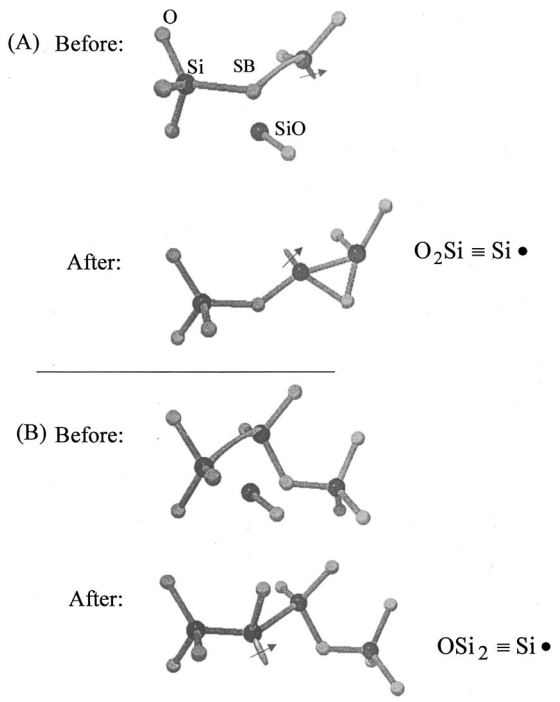

FIG. 12. (a) Speculative picture of thermally driven incorporation of SiO in the a-SiO_2 network at strained bond (SB) sites: transformation of an E'_γ defect into an $O_2Si \equiv Si\cdot$ structure by successively strained bond breaking and incorporation of volatile SiO into the a-SiO_2 network. (b) Breaking of a strained Si-Si bond and incorporation of volatile SiO leading to an $OSi_2 \equiv Si\cdot$ defect.

Finally, then, there remains the basic quest as to the atomic nature of the interaction site. Here one can add little more than speculation. First, one may ponder about its chemical character: it may be either intrinsic in nature—a particular structural feature of (defects in) the SiO_2 network—or extrinsic. In the latter case, it may be related to a particular impurity straightly incorporated in the SiO_2 network (considered unlikely, as mentioned) or, perhaps less directly, a site appearing in the network as a result of the presence or catalytic action of an impurity, either during POVA or oxide formation itself. If so, tracing that impurity (or, perhaps, impurities, should there be more than one type) would be exciting. Here it may not be amiss to reemphasize the crucial role of O_2 in the degradation matter: As long as one stays in the oxidation regime during POA, i.e., $p_{O_2} > 100\, p_{SiO}^{equi}$, no degradation is observed. Clearly, more in-depth research will be required.

Two, to help achieve insight, a relevant observation may be the uncovered general spatial anticorrelation in the occurrence of the S and E'_γ defects (cf. Fig. 3). This may suggest that interacting SiO preferably scavenges Si dangling bond type sites (O vacancies), transforming these then in $Si_nO_{3-n}{\equiv}Si\cdot$ $(n=1,2)$ type centers. It may hint at a route to modeling. One such possibility is depicted in Fig. 12(a), where through SiO incorporation, a (strained) E' site is transformed into a kind of "epoxide" $O_2Si{\equiv}Si\cdot$ defect. Similary, at the site of a strained Si-Si bond, one may picture SiO incorporation to result in $OSi_2{\equiv}Si\cdot$ formation [cf. Fig. 12(b)]

For completeness, we should add that in the oxide layer between 100 and 300 Å from the top oxide surface, E'_γ centers predominate and attain large densities (up to $\sim 3\times10^{18}\,cm^{-3}$). Obviously, then, if E'_γ- and S-center generation compete, in this region the balance must be drastically tipped in favor of the former. Perhaps, this has to do with initial oxide characteristics, referring again to nonuniformity.

V. CONCLUSIONS

Post-oxidation annealing of Si/SiO_2 structures in vacuum in the range 900–1250 °C results in the production of ESR-active point defects in the oxide. Their generation has been studied systematically as a function of T_{an}. Among these defects, the S center, previously reported only once in thermal SiO_2, appears most substantial, especially for $T_{an}\rightarrow1250\,°C$. Other occurring and more familiar defects are E'_γ, E'_δ, and EX. The latter three were only detected after VUV irradiation under positive bias.

The ESR characteristics of the S center, displaying rather unpronounced spectral properties, have been studied in detail, with the aim to identification. Salient (K band) ESR properties include (a) zero crossing $g=2.002\,69\pm0.000\,08$. For one sample, exhibiting a distinct high S density ($\sim1\times10^{15}\,cm^{-2}$) a shift in resonance position was observed as a function of the applied magnet field angle and temperature (4–20 K). These dependences are attributed to demagnetization effects. (b) Approximately Lorentzian shape, apparently slightly asymmetric. (c) For $[S]\lesssim10^{14}\,cm^{-2}$, a peak-to-peak linewidth >6 G. The latter increases with the defect density, but is independent of the microwave frequency. (d) The signal is fairly insensitive to microwave saturation at ~4.3 K: it can endure about ~15 dB higher P_μ than the other more familiar defects in the oxide, i.e., E'_γ, E'_δ, and EX. (e) In the range 4–30 K the magnetic susceptibility is found to be almost purely Curie type, with a constant critical temperature $T_C=\sim1.3$ K, indicating a possible slight trend for ferromagnetic coupling between the spins. (f) For the highest densities attained ($\sim10^{15}\,cm^{-2}$), an intense search for hf structure was carried out, yet with limited success, likely due to excessive hf signal broadening. There is evidence for two distinctly broadened doublets of splitting, ~162 and ~289 G, respectively, the latter being more broadened. Their appearence may comply with a Si-centric defect, yet no decisive prove is provided.

Signal analysis suggests the line shape and linewidth to be dominated by dipolar broadening in addition to other contributions. The subtle asymmetry of the line shape might indicate the presence of g anisotropy. Accordingly, powder pattern line shape simulations were carried out showing that the components of $\hat{g}$ might vary up to $\sim1\times10^{-3}$, without resolving observable powder pattern shape features. Distribution depth profiles of the S and E'_γ defects were mapped for a $T_{an}=1200\,°C$ sample, unveiling two major regions in the oxide layer ($d_{ox}\sim66$ nm), both with respect to etch rate and defect distribution: The top oxide layer (to a depth of 400 Å) etches at 5.5 ± 0.7 Å/s, in agreement with standard data. In the layer of 200–300 Å from the Si/SiO_2 interface, however, a gradual decrease in the etch rate is observed down to ~0.4 Å/s, indicating structural and/or stoichiometric changes towards the interface. Both the S and E'_γ defects are found distinctly inhomogeneously distributed throughout the oxide. The S center is found piled up towards the oxide borders: a sharp pileup, within ~40 Å at the Si/SiO_2 interface, and a more stretched out one towards the outer surface. The 200–300-Å-thick oxide layer near the Si/SiO_2 interface contains almost no ESR defects except for the S-center pileup in the last 40 Å towards the interface. About 50% of the observed S centers reside in the top and bottom ~50-Å-thick layers. Remarkably, the E'_γ centers reside predominantly in the top half of the oxide, with, however, no E'_γ defects in the top ~100 Å layer. No E'_γ defects are found beyond a depth of 400 Å. Apparently, the S and E'_γ distributions are in anticorrelation. During etch-off, no significant changes in the linewidth of the S signal was observed, indicating that, if accepting dipolar broadening as the main line broadening mechanism, the S centers occur clustered.

This study complements the previously unveiled creation of *interface defects* (P_b-type defects) as a result of POVA.[7,9] Both oxide and interface degradation, proceeding in correlation, are related to a previously reported oxide decomposition reaction occurring under high-temperature vacuum conditions. The variety of defects observed in the oxide, i.e., S, E'_γ, E'_δ, and EX, is suggested to be (partly) related to the interaction with the oxide network of volatile SiO, freed from the interface and diffusing through the oxide. A unique relation between the anneal temperature and defect concentration is observed.

From the comparison of the ESR features with known intrinsic oxide defects, the S center is suggested to be a Si dangling bond type defect, possible of the type $O_2Si{\equiv}Si\cdot$ and/or $OSi_2{\equiv}Si\cdot$. The ESR signal properties comply with what can be expected from such Si dangling bond defects. If looking at the $O_2Si{\equiv}Si\cdot$ and $OSi_2{\equiv}Si\cdot$ models as Si-enrichment-related defects in the otherwise stoichiometric SiO_2 network, the assignment is also conceivably in line with the SiO interaction idea, which, as a net result, effectuates Si enrichment of the SiO_2 network. Obviously, the key point then would be to unravel at what sites, e.g., intrinsic or extrinsic in nature, and how SiO is effectively incorporated in the SiO_2 network, to result in the $O_2Si{\equiv}Si\cdot/OSi_2{\equiv}Si\cdot$ type defect formation. This may constitute a very essential clue to insight into thermally induced oxide degradation in O-deficient ambient.

Yet as a final remark it needs to be added that, however detailed the analysis and perhaps being plausible, the $O_2Si{\equiv}Si\cdot$ ($OSi_2{\equiv}Si\cdot$) identification of the *S* center is not considered established. Unambiguous correlation of the unveiled hf structure with the *S* center is lacking. The model, however, is considered as a ''best choice'' working scheme from where to start further verification and, perhaps, implementing improvements. Decisive identification must await, in conjunction with underlying theoretical insight, improved signal intensity, and hf data, including, within the advanced model, detection of the ^{17}O hf structure (probably to be realized through ^{17}O enrichment). Such definite identification may well prove the effort, not only for fundamental reasons. There is also the technological motive, as the *S* defect appears to constitute an essential (if not the main) product of thermally induced degradation in O-deficient ambient of thermal oxide. Unveiling the defect's exact atomic nature may significantly enhance our understanding of the amorphous SiO_2 network.

[1] B. E. Deal, J. Electrochem. Soc. **121**, 198C (1974).
[2] B. E. Deal, J. Electrochem. Soc. **127**, 979 (1980).
[3] T. W. Hickmott, J. Appl. Phys. **48**, 723 (1977).
[4] R. A. B. Devine, D. Mathiot, W. L. Warren, and B. Aspar, J. Appl. Phys. **79**, 2302 (1996).
[5] K. Hofmann, G. W. Rubloff, and D. R. Young, J. Appl. Phys. **61**, 4584 (1987).
[6] A. Stesmans and V. V. Afanas'ev, Appl. Phys. Lett. **69**, 2056 (1996).
[7] A. Stesmans and V. V. Afanas'ev, Phys. Rev. B **54**, R11 129 (1996).
[8] A. Stesmans and V. V. Afanas'ev, Appl. Phys. Lett. **72**, 2271 (1998).
[9] A. Stesmans and V. V. Afanas'ev, J. Vac. Sci. Technol. B **16**, 3108 (1998).
[10] E. H. Poindexter, P. J. Caplan, B. E. Deal, and R. R. Razouk, J. Appl. Phys. **52**, 879 (1981).
[11] D. L. Griscom, E. J. Friebele, K. J. Long, and J. W. Fleming, J. Appl. Phys. **54**, 3443 (1983).
[12] A. Stesmans, Phys. Rev. B **45**, 9501 (1992); A. Stesmans and F. Scheerlinck, *ibid.* **50**, 5204 (1994).
[13] D. L. Griscom, Nucl. Instrum. Methods Phys. Res. B **1**, 481 (1981).
[14] D. L. Griscom and E. J. Friebele, Phys. Rev. B **34**, 7524 (1986).
[15] J. R. Chavez, S. P. Karna, K. Vanheusden, C. P. Brothers, R. D. Pugh, B. K. Singaraju, W. L. Warren, and R. A. B. Devine, IEEE Trans. Nucl. Sci. **NS-44**, 1799 (1997).
[16] S. P. Karna, A. C. Pineda, W. M. Shedd, and B. K. Singaraju, Electrochem. Soc. Proc. **99-3**, 161 (1999).
[17] S. P. Karna, H. A. Kurtz, A. C. Pineda, W. M. Shedd, and R. D. Pugh, in *Defects in SiO_2 and Related Dielectrics: Science and Technology*, edited by G. Pacchioni, L. Skuja, and D. L. Griscom (Kluwer, Dordrecht, 2000), p. 599.
[18] L. Zhang and R. G. Leisure, J. Appl. Phys. **80**, 3744 (1996).
[19] R. Tromp, G. W. Rubloff, P. Balk, F. K. LeGoues, and E. J. van Loenen, Phys. Rev. Lett. **55**, 2332 (1985).
[20] R. E. Walkup and S. I. Raider, Appl. Phys. Lett. **53**, 888 (1988).
[21] Y. Takakuwa, M. Nihei, and N. Miymoto, Jpn. J. Appl. Phys., Part 2 **32**, L480 (1993).
[22] A. Stesmans and V. V. Afanas'ev, Microelectron. Eng. **36**, 201 (1997).
[23] E. Holzenkampfer, F.-W. Richter, J. Stuke, and U. Voget-Grote, J. Non-Cryst. Solids **32**, 327 (1979).
[24] DIMES, Delft, the Netherlands.
[25] G. Van Gorp and A. Stesmans, Phys. Rev. B **45**, 4344 (1992).
[26] A. Stesmans, B. Nouwen, and K. Iakoubovskii, J. Phys.: Condens. Matter **12**, 7807 (2000).
[27] Interference of P_b-type signals is neglible due to saturation.
[28] C. C. Mai and J. C. Looney, SCP and Solid State Technology January 1966, p. 19.
[29] P. M. Marquardt and G. H. Sigel, Jr., IEEE Trans. Nucl. Sci. **NS-22**, 2234 (1975).
[30] K. Brower, Phys. Rev. B **38**, 9657 (1988).
[31] A. Stesmans, Appl. Phys. Lett. **68**, 2723 (1996); **68**, 2076 (1996).
[32] P. Balk, in *Extended Abstracts of the Electrochemical Society Fall Meeting*, (Electrochemical Society, Buffalo, NY, 1965), abstract No. 111, p. 29.
[33] M. L. Reed and J. D. Plummer, J. Appl. Phys. **63**, 5776 (1988).
[34] S. P. Karna and H. A. Kurtz, Microelectron. Eng. **48**, 109 (1999).
[35] S. P. Karna, H. A. Kurtz, W. M. Shedd, R. D. Pugh, and B. K. Singaraju, IEEE Trans. Nucl. Sci. **NS-46**, 1544 (1999).
[36] H. Hosono and R. A. Weeks, Phys. Rev. B **40**, 10 543 (1989).
[37] H. Hosono, H. Kawazoe, K. Oyoshi, and S. Tanaka, J. Non-Cryst. Solids **179**, 39 (1994).
[38] J. H. Van Vleck, Phys. Rev. **74**, 1168 (1948).
[39] C. Kittel and E. Abrahams, Phys. Rev. **90**, 238 (1953).
[40] S. J. Wyard, Proc. Phys. Soc. London **86**, 587 (1965).
[41] G. D. Watkins and J. W. Corbet, Phys. Rev. **134**, A1359 (1964).
[42] K. L. Brower, Phys. Rev. B **33**, 4471 (1986).
[43] A. Stesmans and V. V. Afanas'ev, J. Appl. Phys. **83**, 2449 (1998).
[44] A. Stesmans and J. Braet, in *Insulating Films on Semiconductors*, edited by J. J. Simonne and J. Buxo (North-Holland, Amsterdam, 1986), p. 25.
[45] D. L. Griscom, Phys. Rev. B **20**, 1823 (1979).
[46] See, e.g., C. Kittel, *Introduction to Solid State Physics* (Wiley, New York, 1967).
[47] N. S. VanderVen, Phys. Rev. **168**, 787 (1968).
[48] J. L. Stanger, J. J. André, P. Turek, Y. Hosokoshi, M. Tamura, M. Kinoshita, P. Rey, J. Cirujeda, and J. Veciana, Phys. Rev. B **55**, 8398 (1997).
[49] J. A. Osborn, Phys. Rev. **67**, 351 (1945); D. C. Cronemeyer, J. Appl. Phys. **70**, 2911 (1991).
[50] K. Vanheusden and A. Stesmans, J. Appl. Phys. **69**, 6656 (1991).
[51] M. Stapelbroek, D. L. Griscom, E. J. Friebele, and G. H. Sigel, Jr., J. Non-Cryst. Solids **32**, 313 (1979).
[52] E. J. Friebele, D. L. Griscom, M. A. Stapelbroek, and R. A. Weeks, Phys. Rev. Lett. **42**, 1346 (1979).
[53] D. L. Griscom, Phys. Rev. B **40**, 4224 (1989).
[54] D. L. Griscom, E. J. Friebele, and G. H. Sigel, Jr., Solid State Commun. **15**, 479 (1974).

[55] K. L. Brower, Appl. Phys. Lett. **43**, 1111 (1983).
[56] A. Stesmans, Appl. Surf. Sci. **30**, 134 (1987).
[57] A. Stesmans, J. Appl. Phys. **88**, 489 (2000); Phys. Rev. B **61**, 8393 (2000).
[58] G. K. Celler and L. E. Triamble, Appl. Phys. Lett. **54**, 1427 (1989).
[59] S. T. Ahn, H. W. Kennel, W. A. Tiller, and J. D. Plummer, J. Appl. Phys. **65**, 2957 (1989).
[60] Y.-K. Sun, D. J. Bonser, and T. Engel, J. Vac. Sci. Technol. A **10**, 2314 (1992).
[61] M. E. Zvanut, T. L. Chen, R. E. Stahlbush, E. S. Steigerwalt, and G. A. Brown, J. Appl. Phys. **77**, 4329 (1995).
[62] J. M. Gibson and D. W. Dong, J. Electrochem. Soc. **127**, 2722 (1980); E. A. Irene, J. Appl. Phys. **54**, 5416 (1983).
[63] A. Munkholm, S. Brennau, F. Comin, and L. Ortega, Phys. Rev. Lett. **75**, 4254 (1995).
[64] D. L. Griscom, J. Appl. Phys. **58**, 2524 (1985); A. G. Revesz, J. Electrochem. Soc. **126**, 122 (1979); R. Gale, F. J.-Feigl, C. W. Magee, and D. R. Young, J. Appl. Phys. **54**, 6938 (1983).
[65] P. M. Lenahan, J. F. Conley, Jr., and B. D. Wallace, J. Appl. Phys. **81**, 6822 (1997).